Magnetic field assisted transmission of THz waves through a graphene layer combined with a periodically perforated metallic film

Yu. V. Bludov,* M. I. Vasilevskiy, and N. M. R. Peres
Departmento de Física and Centro de Física, Universidade do Minho, PT-4710-057, Braga, Portugal
and QuantaLab, University of Minho, PT-4710-057, Braga, Portugal

(Received 13 October 2017; revised manuscript received 5 January 2018; published 31 January 2018)

We consider a graphene sheet encapsulated in a two-dimensional (2D) metallic grating and a substrate (Al_2O_3) and subjected to an external magnetic field (in Faraday configuration). The grating consists of a thin perfectly conducting metal film perforated with a 2D periodic array of square holes. According to our calculations, significant changes in the spectra of the Faraday rotation angle of the transmitted wave and of the magnetic circular dichroism should be expected in this situation compared to bare graphene. We explain this enhancement by the excitation of graphene magnetoplasmons that accompanies the transmission of the electromagnetic wave through the structure. The results can be interesting for applications in THz photonics, such as switchable rotating polarizer and optical isolator.

DOI: 10.1103/PhysRevB.97.045433

I. INTRODUCTION

One of the prominent features of the magnetoactive structures is a strong dependence of the electromagnetic wave characteristics upon the direction of propagation. An illustrative example is the Faraday effect [1], where the direction of the rotation of the plane of polarization is different for the forward- and backward-proparating waves in magnetoactive media along the direction of static external magnetic field (Faraday geometry). Similar phenomenon—nonreciprocal phase shift [2,3]—takes place in asymmetric structures [4] (e.g., waveguides) when the direction of propagation is perpendicular to the magnetic field (Voigt geometry). These phenomena constitute the basis for the operation principles of a variety of microwave photonic devices, such as optical isolators [5,6], circulators [7,8], and switches [9,10] (for a review on practical application of magneto-optical materials, see Refs. [11,12]).

The general tendency to the minituarization of the photonic components resulted in the creation of magnetoptical devices, which key building blocks are photonic crystals [13–20] or electromagnetic metasurfaces [21,22]. Yet, the diffraction limit of electromagnetic waves imposes one of the fundamental obstacles for further minituarization and growth of integration of photonic devices in optoelectronics circuitry. One of the possible ways to circumvent this limit is to build the photonic components, whose operation principles are based on the surface electromagnetic waves instead of on their free space counterparts. To be specific, incorporating metallic structures into a photonic platform allows one to create circuitry, operating on *surface plasmon polaritons*—a special kind of the electromagnetic waves, whose energy is localized near the metal-dielectric interface and whose wavelength is considerably smaller than that of the free space wave with the same frequency [23,24].

Combining plasmonics with magneto-optics [25,26] gives a variety of advantages [27]. First, magnetic field allows to achieve the dynamical tunability (control of parameters in real time) of plasmonic structure [28–31]. Second, the aforementioned phenomenon of the nonreciprocal propagation allows to create plasmonic analogues of different magneto-optical devices [32–34]. Third, the resonant excitation of the magnetoplasmons and their coupling to the transmitted and reflected bulk waves results in a significant enhancement of the Faraday and magneto-optical Kerr effects [35–38]. However, introducing the magneto-optical materials into the plasmonic circuitry enhances significantly the losses in the system, thus reducing the free path of magnetoplasmons (compared to the conventional plasmonic structures). As a result, nowadays there is a huge demand for novel magnetoplasmonic materials.

In the context discussed above, graphene emerges as a promising candidate, operating in the THz and mid-IR spectral range. This material possesses several properties, which can be advantageous for the magneto-optics and magnetoplasmonics. To begin with, surface plasmon polaritons in graphene [39–43] are characterized by both large lifetime and high degree of field confinement [44,45]. Simultaneously, graphene is a magnetoactive material: being subjected to an external static magnetic field (perpendicular to its surface), graphene exhibits some unusual magnetic properties, such as the Hall effect at room temperture [46,47] or confinement of the Dirac-Weyl quasiparticles by a magnetic barrier [48]. Furthermore, its conductivity (and, consequently, its transmittance and the reflectance [49–53] as well as the dispersion properties of magnetoplasmons [54–57]) can be effectively tuned by changing the applied magnetic field. The possibility to achieve the magnetoplasmon-mediated enhancement of the magneto-optical phenomena was demonstrated in various graphene-based structures, such as a periodic array of graphene ribbons [58], a graphene monolayer patterned with the periodical antidot array [59], an array of graphene-covered nanowires [60], or a monolayer graphene metasurface [61].

*bludov@fisica.uminho.pt

In this paper we study the interaction of a THz electromagnetic wave with a graphene monolayer cladded by a semi-infinite substrate and a periodically perforated metallic film of finite thickness. This metallic film is assumed made of a perfect metal and containing a two-dimensional (2D) periodic array of square holes. The structure is subjected to an external magnetic field directed perpendicularly to the surface (Faraday geometry). We demonstrate that if the two-dimensional metallic grating is sparse enough, it screens the incident long-wavelength electromagnetic wave. As a result, in the low-frequency range the Faraday rotation in the graphene covered with the perforated metal film is less than that in the graphene layer alone. At high frequencies, the sparse metallic grating almost does not influence the propagation of the electromagnetic wave. At the same time, in the intermediate frequency range the diffraction of the incident electromagnetic wave on the grating results in the excitation of graphene magnetoplasmons. This process increases considerably the Faraday rotation angle of the polarization vector for a linearly polarized wave. For a circularly polarized propagating wave, the presence of the perforated metallic film leads to inversion of the sign of the magnetic circular dichroism (MCD) in the low-frequency range.

The paper is organized as follows. In Sec. II we obtain the principal equations governing the process of incident wave diffraction on graphene combined with the periodical array of holes in the metal film. Section III is devoted to a detailed discussion of how the parameters of this structure influence the Faraday rotation angle of the transmitted electromagnetic wave. In Sec. IV we investigate the magnetic circular dichroism in this structure. The conclusions are presented in Sec. V.

II. DIFFRACTION OF PLANE ELECTROMAGNETIC WAVE ON METAL FILM WITH PERIODIC ARRAY OF HOLES

We consider a perfectly conducting metal film of thickness d (whose film surfaces are situated at planes $z = \pm d/2$, see Fig. 1), containing a periodic array of square holes, each of width W, arranged at $lD < x < lD + W$, $l'D < y < l'D + W$ and forming a square lattice. Here D is the period of the square lattice and l, l' are the hole indices. We also assume that this metallic grating is deposited on top of a graphene monolayer, arranged at the plane $z = d/2$. The graphene monolayer is deposited on top of a semi-infinite dielectric substrate (Al_2O_3) occupying the half-space $z > d/2$ and characterized by the dielectric function ε. The plane wave impinges on the metal grating from air (the half-space $z < -d/2$) at normal incidence.

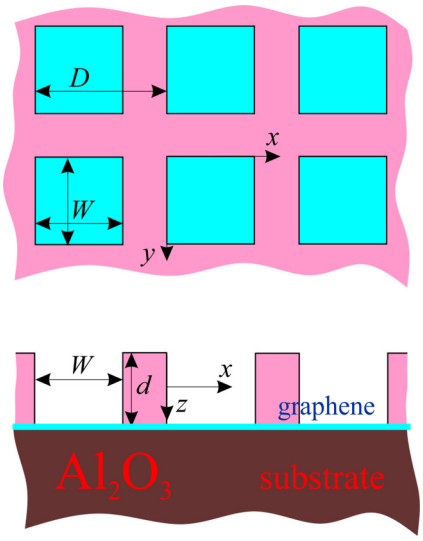

FIG. 1. Two-dimensional periodic array of holes in metallic film deposited on top of a graphene layer covering a dielectric substrate.

The periodicity of the structure in the directions x and y, as well as the normal incidence of the external wave impose the requirement for the solution of Maxwell equations to be also periodic. In half-spaces $z < -d/2$ and $z > d/2$ (vacuum and substrate) electromagnetic fields can be represented in the form of Fourier series with respect to the lattice vector $g = 2\pi/D$, namely

$$\begin{pmatrix} H_x^{(1)}(\mathbf{r},z) \\ H_y^{(1)}(\mathbf{r},z) \\ E_x^{(1)}(\mathbf{r},z) \\ E_y^{(1)}(\mathbf{r},z) \end{pmatrix} = \begin{pmatrix} \hat{\mathcal{I}} \\ i\hat{\sigma}_y \end{pmatrix} \begin{pmatrix} H_x^{(i)} \\ H_y^{(i)} \end{pmatrix} \exp\left[ip_{0,0}^{(1)}(z + d/2)\right] + \sum_{s,j=-\infty}^{\infty} \begin{pmatrix} \hat{\mathcal{I}} \\ -\hat{\mathcal{Q}}_{s,j}^{(1)} \end{pmatrix} \begin{pmatrix} H_{x||s,j}^{(r)} \\ H_{y||s,j}^{(r)} \end{pmatrix} \exp\left[i\mathbf{k}_{s,j}\mathbf{r} - ip_{s,j}^{(1)}(z + d/2)\right], \quad (1)$$

$$\begin{pmatrix} H_x^{(3)}(\mathbf{r},z) \\ H_y^{(3)}(\mathbf{r},z) \\ E_x^{(3)}(\mathbf{r},z) \\ E_y^{(3)}(\mathbf{r},z) \end{pmatrix} = \sum_{s,j=-\infty}^{\infty} \begin{pmatrix} \hat{\mathcal{I}} \\ \hat{\mathcal{Q}}_{s,j}^{(3)} \end{pmatrix} \begin{pmatrix} H_{x||s,j}^{(t)} \\ H_{y||s,j}^{(t)} \end{pmatrix} \exp\left[i\mathbf{k}_{s,j}\mathbf{r} + ip_{s,j}^{(3)}(z - d/2)\right], \quad (2)$$

where s, j stand for the indices of spatial harmonics, and $\mathbf{k}_{s,j} = (sg, jg)$ is the 2D wave vector in the transverse plane $\mathbf{r} = (x, y)$. The spatial dependence of the field components in Eqs. (1) and (2) is represented by the common exponential factors, multiplied by 2×1 matrices of the magnetic field amplitudes $(H_{x||s,j}^{(i)}, H_{y||s,j}^{(i)})^T$, $(H_{x||s,j}^{(r)}, H_{y||s,j}^{(r)})^T$, and $(H_{x||s,j}^{(t)}, H_{y||s,j}^{(t)})^T$. In turn, these amplitude matrices are multiplied by 4×2 block matrices, represented by the following 2×2 elements:

$$\hat{\mathcal{I}} = \begin{pmatrix} 1 & 0 \\ 0 & 1 \end{pmatrix}$$

is the unity matrix,

$$\hat{\sigma}_y = \begin{pmatrix} 0 & -i \\ i & 0 \end{pmatrix}$$

is the Pauli matrix,

$$\hat{\mathcal{Q}}^{(1)}_{s,j} = \begin{pmatrix} \frac{c}{\omega}\frac{sjg^2}{p^{(1)}_{s,j}} & \frac{c}{\omega}\frac{(p^{(1)}_{s,0})^2}{p^{(1)}_{s,j}} \\ -\frac{c}{\omega}\frac{(p^{(1)}_{0,j})^2}{p^{(1)}_{s,j}} & -\frac{c}{\omega}\frac{sjg^2}{p^{(1)}_{s,j}} \end{pmatrix},$$

$$\hat{\mathcal{Q}}^{(3)}_{s,j} = \begin{pmatrix} \frac{c}{\omega\varepsilon}\frac{sjg^2}{p^{(3)}_{s,j}} & \frac{c}{\omega\varepsilon}\frac{(p^{(3)}_{s,0})^2}{p^{(3)}_{s,j}} \\ -\frac{c}{\omega\varepsilon}\frac{(p^{(3)}_{0,j})^2}{p^{(3)}_{s,j}} & -\frac{c}{\omega\varepsilon}\frac{sjg^2}{p^{(3)}_{s,j}} \end{pmatrix},$$

and $p^{(1)}_{s,j} = \sqrt{(\omega/c)^2 - |\mathbf{k}_{s,j}|^2}$, $p^{(3)}_{s,j} = \sqrt{(\omega/c)^2\varepsilon - |\mathbf{k}_{s,j}|^2}$ are z components of the wave vector, corresponding to (s,j) harmonics in the vacuum and substrate, respectively. Also in Eqs. (1) and (2) the electromagnetic field time-dependence is implicitly assumed as $\mathbf{E},\mathbf{H} \sim \exp(-i\omega t)$.

Equations (1) and (2) can be interpreted in the following manner. In the half-space $z < -d/2$, occupied by air, the total electromagnetic field is composed of the electromagnetic fields, which correspond to incident [first term in Eq. (1)] and reflected [second term in Eq. (1)] waves. At the same time, in the substrate (half-space $z > d/2$) electromagnetic field [see Eq. (2)] contains the transmitted wave only. If the sign of the wave vector's z component $p^{(n)}_{s,j}$ (where $n = 1,3$) satisfies the conditions $\mathrm{Re}(p^{(n)}_{s,j}) \geqslant 0$, $\mathrm{Im}(p^{(n)}_{s,j}) \geqslant 0$, the transverse incident wave propagates along z axis in the positive direction and is characterized by the wave vector $p^{(1)}_{0,0} = \omega/c$ and the magnetic field amplitude $\mathbf{H}^{(i)} = (H^{(i)}_x, H^{(i)}_y, 0)$. The reflected and transmitted waves contain an infinite number of spatial harmonics. The reflected wave harmonic with index (s,j) [characterized by the amplitude $\mathbf{H}^{(r)}_{s,j} = (H^{(r)}_{x||s,j}, H^{(r)}_{y||s,j}, H^{(r)}_{z||s,j})$ and 3D wave vector $(\mathbf{k}_{s,j}, -p^{(1)}_{s,j})$] in the negative direction of z axis can be either propagating wave (in this case $|\mathbf{k}_{s,j}| < \omega/c$ and $p^{(1)}_{s,j}$ will be purely real and positive) or evanescent (in this case $|\mathbf{k}_{s,j}| > \omega/c$ and $p^{(1)}_{s,j}$ will be purely imaginary and positive). Owing to the fact that substrate's dielectric constant ε is complex, each of the transmitted wave harmonics s,j [with amplitude $\mathbf{H}^{(t)}_{s,j} = (H^{(t)}_{x||s,j}, H^{(t)}_{y||s,j}, H^{(t)}_{z||s,j})$ and 3D wave vector $(\mathbf{k}_{s,j}, p^{(3)}_{s,j})$] is of mixed type: along z axis it propagates in its positive direction with exponential factor $\sim\exp[i\mathrm{Re}(p^{(3)}_{s,j})z]$, but having a decaying amplitude $\sim\exp[-\mathrm{Im}(p^{(3)}_{s,j})z]$.

Inside the holes in the metallic film, for $lD < x < lD + W, l'D < y < l'D + W, -d/2 \leqslant z \leqslant d/2$, transverse components of the magnetic and electric fields can be represented in matrix form as (see Appendix A 1 for details)

$$\begin{pmatrix} H^{(2)}_x(\mathbf{r},z) \\ H^{(2)}_y(\mathbf{r},z) \end{pmatrix} = \sum_{m,n=0}^{\infty} \hat{\mathcal{P}}_{m,n}(x - lD, y - l'D)\hat{U}_{m,n} \left\{ \begin{pmatrix} A^{(s)}_{m,n}\delta'_{m,0}\delta'_{0,n} \\ B^{(s)}_{m,n} \end{pmatrix} \sin\left[\mu_{m,n}\left(z + \frac{d}{2}\right)\right] + \begin{pmatrix} A^{(c)}_{m,n}\delta'_{m,0}\delta'_{0,n} \\ B^{(c)}_{m,n} \end{pmatrix} \cos\left[\mu_{m,n}\left(z - \frac{d}{2}\right)\right] \right\}, \tag{3}$$

$$\begin{pmatrix} E^{(2)}_x(\mathbf{r},z) \\ E^{(2)}_y(\mathbf{r},z) \end{pmatrix} = \sum_{m,n=0}^{\infty} \hat{\mathcal{P}}'_{m,n}(x - lD, y - l'D)\hat{U}_{m,n} \left\{ \begin{pmatrix} B^{(s)}_{m,n} \\ A^{(s)}_{m,n}\delta'_{m,0}\delta'_{0,n} \end{pmatrix} \cos\left[\mu_{m,n}\left(z + \frac{d}{2}\right)\right] - \begin{pmatrix} B^{(c)}_{m,n} \\ A^{(c)}_{m,n}\delta'_{m,0}\delta'_{0,n} \end{pmatrix} \sin\left[\mu_{m,n}\left(z - \frac{d}{2}\right)\right] \right\}, \tag{4}$$

where the coefficients are 2×2 matrices

$$\hat{\mathcal{P}}_{m,n}(\xi,\eta) = \begin{pmatrix} \sin\left(\frac{m\pi}{W}\xi\right)\cos\left(\frac{n\pi}{W}\eta\right) & 0 \\ 0 & \cos\left(\frac{m\pi}{W}\xi\right)\sin\left(\frac{n\pi}{W}\eta\right) \end{pmatrix},$$

$$\hat{\mathcal{P}}'_{m,n}(\xi,\eta) = \hat{\sigma}_x\hat{\mathcal{P}}_{m,n}(\xi,\eta)\hat{\sigma}_x = \begin{pmatrix} \cos\left(\frac{m\pi}{W}\xi\right)\sin\left(\frac{n\pi}{W}\eta\right) & 0 \\ 0 & \sin\left(\frac{m\pi}{W}\xi\right)\cos\left(\frac{n\pi}{W}\eta\right) \end{pmatrix},$$

$$\hat{U}_{m,n} = \frac{W}{(m^2+n^2)\pi}\begin{pmatrix} -\frac{i\omega}{c}n & m\mu_{m,n} \\ \frac{i\omega}{c}m & n\mu_{m,n} \end{pmatrix},$$

where m and n are the mode indices, $A^{(c)}_{m,n}$, $A^{(s)}_{m,n}$ are the amplitudes of E-modes, while $B^{(c)}_{m,n}$, $B^{(s)}_{m,n}$ are the H-modes amplitudes. In general, E-modes inside the square hole exist for nonzero mode indices $m,n \geqslant 1$—this is taken into account in Eqs. (3) and (4) introducing the factor $\delta'_{m,0}\delta'_{0,n}$ in front of the E-mode coefficients (where $\delta'_{m,n} = 1 - \delta_{m,n}$ and $\delta_{m,n}$ is the Kronecker δ). On the other hand, the H-mode index (m or n) can be zero—excepting the case when both indices $m = n = 0$, and this term is implicitly excluded from the summation in Eqs. (3) and (4). Notice that Eqs. (3) and (4)

satisfy the boundary conditions, namely, zero tangential components of the electric field and zero normal components of the magnetic field on the metal surfaces, $E_x^{(2)}(x,l'D,z) = H_y^{(2)}(x,l'D,z) = 0$, $E_x^{(2)}(x,l'D+W,z) = H_y^{(2)}(x,l'D+W,z) = 0$, $E_y^{(2)}(lD,y,z) = H_x^{(2)}(lD,y,z) = 0$, $E_y^{(2)}(lD+W,y,z) = H_x^{(2)}(lD+W,y,z) = 0$. Along with this, the periodicity of the solutions of Eqs. (3) and (4) is achieved through the independence of the mode amplitudes upon the hole indices l,l'.

The electromagnetic fields in the regions $z < -d/2$, $-d/2 < z < d/2$, and $z > d/2$ are mutually coupled through the boundary conditions. Thus, at the surface of the perforated metal film where graphene is absent ($z = -d/2$), boundary conditions for the electric field tangential components can be represented as

$$\begin{pmatrix} E_x^{(1)}(\mathbf{r},-d/2) \\ E_y^{(1)}(\mathbf{r},-d/2) \end{pmatrix} = \begin{cases} \begin{pmatrix} E_x^{(2)}(\mathbf{r},-d/2) \\ E_y^{(2)}(\mathbf{r},-d/2) \end{pmatrix} & lD \leqslant x \leqslant lD+W, \\ 0, & l'D \leqslant y \leqslant l'D+W, \\ & \text{otherwise.} \end{cases} \tag{5}$$

The physical meaning of Eq. (5) is as follows: at the area of the holes the tangential components of the electric field are continuous across the vertical interface $z = -d/2$. Beyond the area of the holes (at the surface of the metal) the electric field tangential components vanish. Similarly, for the tangential components of the magnetic field, we have

$$\begin{pmatrix} H_x^{(1)}(\mathbf{r},-d/2) \\ H_y^{(1)}(\mathbf{r},-d/2) \end{pmatrix} = \begin{pmatrix} H_x^{(2)}(\mathbf{r},-d/2) \\ H_y^{(2)}(\mathbf{r},-d/2) \end{pmatrix}, \quad \begin{matrix} lD \leqslant x \leqslant lD+W, \\ l'D \leqslant y \leqslant l'D+W. \end{matrix} \tag{6}$$

Notice that Eq. (6) is defined on the hole area only.

At the opposite metal surface, $z = d/2$ (where graphene is present) the boundary conditions for the electric field are the same as those described by Eq. (5). At the same time, magnetic field tangential components are discontinuous across the graphene sheet due to the presence of induced currents (see Appendix A 2 for details):

$$\begin{pmatrix} H_x^{(3)}(\mathbf{r},d/2) \\ H_y^{(3)}(\mathbf{r},d/2) \end{pmatrix} + \hat{\mathcal{G}} \begin{pmatrix} E_x^{(2)}(\mathbf{r},d/2) \\ E_y^{(2)}(\mathbf{r},d/2) \end{pmatrix} = \begin{pmatrix} H_x^{(2)}(\mathbf{r},d/2) \\ H_y^{(2)}(\mathbf{r},d/2) \end{pmatrix}, \quad \begin{matrix} lD \leqslant x \leqslant lD+W, \\ l'D \leqslant y \leqslant l'D+W, \end{matrix} \tag{7}$$

where

$$\hat{\mathcal{G}} = \frac{4\pi}{c} \begin{pmatrix} -\Sigma_{yx} & -\Sigma_{yy} \\ \Sigma_{xx} & \Sigma_{xy} \end{pmatrix} \tag{8}$$

is a 2×2 matrix and Σ_{xx}, Σ_{xy}, Σ_{yx}, Σ_{yy} are the components of the graphene conductivity tensor [62] in magnetic field (see Appendix A 2).

Substituting explicit expressions for the electromagnetic fields Eqs. (1)–(4) into boundary conditions Eqs. (5)–(7) and using the orthogonality of the respective eigenmodes (details can be found in Appendix A 2), one can obtain the following system of equations for the eigenmode amplitudes:

$$\hat{\mathcal{P}}_{m',n'||0,0} \begin{pmatrix} H_x^{(i)} \\ H_y^{(i)} \end{pmatrix} + \sum_{s,j=-\infty}^{\infty} \hat{\mathcal{P}}_{m',n'||s,j} \begin{pmatrix} H_{x||s,j}^{(r)} \\ H_{y||s,j}^{(r)} \end{pmatrix} = \begin{pmatrix} \delta'_{m',0}(1+\delta_{0,n'}) & 0 \\ 0 & \delta'_{0,n'}(1+\delta_{m',0}) \end{pmatrix} \frac{W^2}{4} \hat{U}_{m',n'} \begin{pmatrix} A_{m',n'}^{(c)} \delta'_{m',0}\delta'_{0,n'} \\ B_{m',n'}^{(c)} \end{pmatrix} \cos(\mu_{m',n'}d); \tag{9}$$

$$\sum_{s,j=-\infty}^{\infty} \hat{\mathcal{P}}_{m',n'||s,j} \left(\hat{I} + \hat{\mathcal{G}}\hat{\mathcal{Q}}_{s,j}^{(3)}\right) \begin{pmatrix} H_{x||s,j}^{(t)} \\ H_{y||s,j}^{(t)} \end{pmatrix}$$

$$= \begin{pmatrix} \delta'_{m',0}(1+\delta_{0,n'}) & 0 \\ 0 & \delta'_{0,n'}(1+\delta_{m',0}) \end{pmatrix} \frac{W^2}{4} \hat{U}_{m',n'} \begin{pmatrix} \left[A_{m',n'}^{(s)} \sin(\mu_{m',n'}d) + A_{m',n'}^{(c)}\right] \delta'_{m',0}\delta'_{0,n'} \\ B_{m',n'}^{(s)} \sin(\mu_{m',n'}d) + B_{m',n'}^{(c)} \end{pmatrix}, \tag{10}$$

$$i\hat{\sigma}_y \begin{pmatrix} H_x^{(i)} \\ H_y^{(i)} \end{pmatrix} D^2 \delta_{s',0}\delta_{j',0} - D^2 \hat{\mathcal{Q}}_{s',j'}^{(1)} \begin{pmatrix} H_{x||s,j}^{(r)} \\ H_{y||s,j}^{(r)} \end{pmatrix} = \sum_{m,n=0}^{\infty} \overline{\hat{\mathcal{P}}_{n,m||j',s'}} \hat{U}_{m,n} \begin{pmatrix} B_{m,n}^{(s)} + B_{m,n}^{(c)} \sin(\mu_{m,n}d) \\ \left[A_{m,n}^{(s)} + A_{m,n}^{(c)} \sin(\mu_{m,n}d)\right] \delta'_{m,0}\delta'_{0,n} \end{pmatrix}, \tag{11}$$

$$D^2 \hat{\mathcal{Q}}_{s',j'}^{(3)} \begin{pmatrix} H_{x||s',j'}^{(t)} \\ H_{y||s',j'}^{(t)} \end{pmatrix} = \sum_{m,n=0}^{\infty} \overline{\hat{\mathcal{P}}_{n,m||j',s'}} \hat{U}_{m,n} \begin{pmatrix} B_{m,n}^{(s)} \\ A_{m,n}^{(s)} \delta'_{m,0}\delta'_{0,n} \end{pmatrix} \cos(\mu_{m,n}d), \tag{12}$$

where

$$\hat{\mathcal{P}}_{m',n'||s,j} = \int_0^W dx \int_0^W dy \hat{\mathcal{P}}_{m,n}(\mathbf{r}) \exp[i\mathbf{k}_{s,j}\mathbf{r}] = \begin{pmatrix} S_{m'||s}C_{n'||j} & 0 \\ 0 & C_{m'||s}S_{n'||j} \end{pmatrix},$$

$$\overline{\hat{\mathcal{P}}_{n,m||j',s'}} = \int_0^W dx \int_0^W dy \hat{\mathcal{P}}'_{m,n}(\mathbf{r}) \exp[-i\mathbf{k}_{s,j}\mathbf{r}] = \begin{pmatrix} \overline{C_{m||s'}S_{n||j'}} & 0 \\ 0 & \overline{S_{m||s'}C_{n||j'}} \end{pmatrix},$$

$C_{m||s} = \int_0^W \cos(\frac{m\pi}{W}x)\exp(isgx)dx$, $S_{m||s} = \int_0^W \sin(\frac{m\pi}{W}x)\exp(isgx)dx$ and the overbar stands for the complex conjugation. Thus, solving the linear system of Eqs. (9)–(12), it is possible to obtain the amplitudes of the excited modes inside the holes as well as amplitudes of the reflected and transmitted harmonics. From these it is possible to calculate the total reflectance R and transmittace T of the structure as [see Appendix A 3 for details]

$$R = -\left[\left|H_x^{(i)}\right|^2 + \left|H_y^{(i)}\right|^2\right]^{-1} \sum_{i,j=-\infty}^{\infty} \mathrm{Re}\left\{ \begin{pmatrix} H^{(r)}_{x||s,j} \\ H^{(r)}_{y||s,j} \end{pmatrix}^{\dagger} i\hat{\sigma}_y \hat{Q}^{(1)}_{s,j} \begin{pmatrix} H^{(r)}_{x||s,j} \\ H^{(r)}_{y||s,j} \end{pmatrix} \right\}, \tag{13}$$

$$T = -\left[\left|H_x^{(i)}\right|^2 + \left|H_y^{(i)}\right|^2\right]^{-1} \sum_{i,j=-\infty}^{\infty} \mathrm{Re}\left\{ \begin{pmatrix} H^{(t)}_{x||s,j} \\ H^{(t)}_{y||s,j} \end{pmatrix}^{\dagger} i\hat{\sigma}_y \hat{Q}^{(3)}_{s,j} \begin{pmatrix} H^{(t)}_{x||s,j} \\ H^{(t)}_{y||s,j} \end{pmatrix} \right\}. \tag{14}$$

It is common to characterize the transmission of graphene-based structures in terms of the so called extinction relative to bare graphene with zero Fermi energy (designated by the abbreviation CNP that stands for "charge neutrality point") [59], $1 - T/T_{\mathrm{CNP}}$, where both transmittances can be calculated using the above equation. We shall present this quantity calculated in the subsequent sections.

III. FARADAY ROTATION

One of the principal goals of the present work is to investigate the influence of the magnetoplasmon resonance on the Faraday rotation of an electromagnetic wave traversing the graphene layer. To clarify the role of magnetoplasmons in the Faraday rotation, we start this section by briefly considering the dispersion properties of magnetoplasmons.

A. Magnetoplasmons in graphene

The dispersion relation of magnetoplasmons $k(\omega)$ can be obtained from the following equation (see Appendix B 1 for details):

$$\left[p^{(3)}(k) + \frac{4\pi\omega}{c^2}\sigma_{xx} + p^{(1)}(k)\right] \times \left[\frac{\varepsilon}{p^{(3)}(k)} + \frac{1}{p^{(1)}(k)} + \frac{4\pi}{\omega}\sigma_{xx}\right] + \left(\frac{4\pi}{c}\sigma_{xy}\right)^2 = 0, \tag{15}$$

where $p^{(1)}(k) = \sqrt{(\omega/c)^2 - k^2}$, $p^{(3)}(k) = \sqrt{(\omega/c)^2\varepsilon - k^2}$ and, similar to the previous section we require $\mathrm{Re}\{p^{(n)}(k)\} \geqslant 0$, $\mathrm{Im}\{p^{(n)}(k)\} \geqslant 0$ $(n = 1,3)$. If we suppose that both the substrate and the graphene layer are lossless [$\mathrm{Im}(\varepsilon) \equiv 0$, $\gamma \equiv 0$], then the dispersion relation Eq. (15) possesses a solution in terms of purely real frequency ω and wave vector k. The magnetoplasmon dispersion is depicted in Figs. 2(a) and 2(b) for low and high magnetic fields, respectively. When the external perpendicular magnetic field is applied to graphene, the magnetoplasmon spectrum contains a low-frequency gap and the magnetoplasmons exist at frequencies higher than a threshold frequency ω_{th} (which is approximately equal to the cyclotron frequency, $\omega > \omega_{\mathrm{th}} \approx \omega_c = e^2 v_F B/\mu$) and for the wave vectors larger than the corresponding threshold wave vector k_{th}. At the threshold frequency, which is equal to 4.85 meV in Fig. 2(a) and 25.6 meV in Fig. 2(b), the magnetoplasmon spectrum splits off from the substrate light line, $k = \omega\sqrt{\varepsilon}/c$, depicted by green dashed lines. Consequently, the value of the wave vector threshold is $k_{\mathrm{th}} = \omega_{\mathrm{th}}\sqrt{\varepsilon}/c$). For higher frequencies, the magnetoplasmon spectrum lies above the light line in the substrate and it results in purely imaginary $p^{(3)}(k)$ and $p^{(1)}(k)$, which determine the localization of the electromagnetic field of the magnetoplasmon close to the graphene layer. Notice that the real part of the substrate dielectric constant

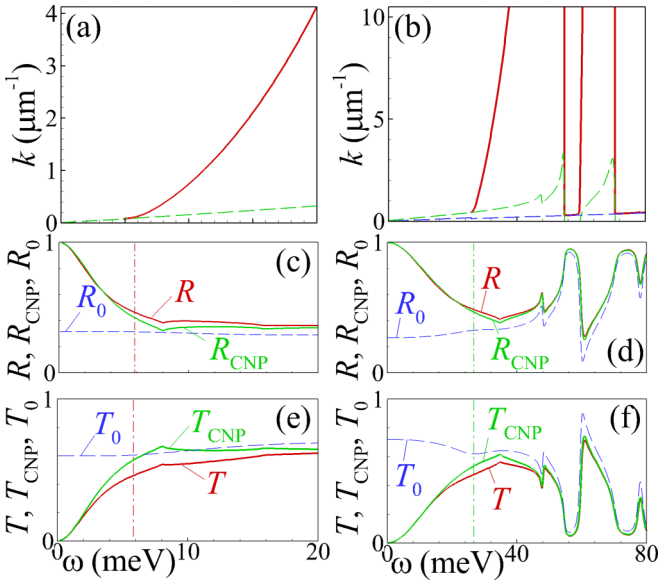

FIG. 2. (a), (b) Dispersion relation of magnetoplasmons (solid red lines) in graphene with the Fermi energy $\mu = 0.175$ eV placed into magnetic field with magnitude $B = 1.5$ T (a) or $B = 7$ T (b). Light lines in vacuum $k = \omega/c$ and in the substrate $k = \omega\sqrt{\varepsilon}/c$ are depicted by blue and green dashed lines, respectively; (c)–(f) Frequency dependence of the reflectance [panels (c) and (d)] and transmittance [panels (e) and (f)] of doped ($\mu = 0.175$ eV, solid red lines) or undoped ($\mu = 0$ eV, green solid lines) graphene placed into the magnetic field and cladded between metal film with square grating of thickness $d = 50$ nm and semi-infinite Al_2O_3 substrate as well as doped ($\mu = 0.175$ eV) graphene without grating ($d = 0$ nm, dashed blue lines). Vertical dash-and-dotted lines depict the frequencies of the magnetoplasmon resonance ω_{mp} for wave vector $k = 2\pi/D$. Other parameters of the structure are: $B = 1.5$ T, $D = 50\,\mu$m [panels (c) and (e)], $B = 7$ T, $D = 10\,\mu$m [panels (d) and (f)], $W = 0.9\,D$, $\gamma = 7.54$ meV. The subscript 0 refers to doped graphene without grating and CNP stands for "charge neutrality point" and means undoped graphene with grating.

is positive [Re(ε) > 0], in this low-frequency range $\omega \gtrsim \omega_{\rm th}$. The physical reason for the existence of magnetoplasmons is the coupling of the electromagnetic wave with excitations of free charge-carriers in graphene.

It is important to notice that in the frequency ranges 55 meV $\lesssim \omega \lesssim$ 60 meV and $\omega \gtrsim$ 70.6 meV [inside the limits of the horizontal axis of Fig. 2(b)] the real part of the substrate dielectric constant is negative [Re(ε) < 0] owing to the excitations of optical phonons [63]. Consequently, in these frequency ranges the physical reason for the existence of surface waves is somewhat different since the substrate-air interface is able to sustain surface modes due to coupling of the electromagnetic wave to the substrate phonons rather than because of the interaction with the free electron oscillations in graphene (in the following these modes will be referred to as surface phonon-polaritons). In this case, the polariton dispersion curve lies above the light line in vacuum $k = \omega/c$ [blue dashed lines in Fig. 2(b)].

B. Magnetoplasmon-enhanced Faraday rotation

The mismatch between the wave vectors of magnetoplasmons and the light line (either in the substrate or in air) determines the impossibility to excite magnetoplasmons by a propagating electromagnetic wave, falling directly onto the graphene layer. One way to overcome this wave-vector mismatch is to use the electromagnetic wave diffraction on some kind of periodic structure added to the graphene layer. In this case the electromagnetic wave diffraction on the periodic structure gives rise to a variety of harmonics [in Eqs. (1) and (2) their 2D wave vectors are $\mathbf{k}_{s,j} = (sg, jg)$]. If at a certain frequency $\omega_{\rm mp}$ the wave vector of one of them coincides with that of the magnetoplasmon spectrum Eq. (15), then the energy of the external electromagnetic wave can be effectively transferred into the energy of the excited magnetoplasmon.

It can be understood from Figs. 2(c)–2(f) that the presence of the perforated metal film on top of the graphene layer modifies significantly the reflectance and transmittance of the structure both in the case of doped (solid red lines) and undoped (solid green lines) graphene. The incident wave is considered to be linearly polarized with the magnetic field along the x axis (i.e., $H_x^{(i)} \neq 0$, $H_y^{(i)} \equiv 0$). For the parameters of Figs. 2(c) and 2(e) the lattice vector is equal to $g = 2\pi/D \approx 0.126\,\mu\text{m}^{-1}$, for which the predicted frequency of the magnetoplasmon resonance [for $k = g$ see Fig. 2(a)] is $\omega_{\rm mp} \approx 5.85$ meV. Similarly, for the parameters of Figs. 2(d) and 2(f) the lattice vector is $g \approx 0.628\,\mu\text{m}^{-1}$ and the magnetoplasmon resonance frequency is $\omega_{\rm mp} \approx 26.75$ meV [which can be obtained from Fig. 2(b)]. In the low-frequency range, $\omega \ll \omega_{\rm mp}$, the wavelength of the incident electromagnetic wave exceeds significantly the period of the grating, $\lambda = 2\pi c/\omega \gg D$. As a result, the perforated metal film screens the incident wave almost like a continuous metal as evidenced by the enhanced reflectance of the structure, $R \lesssim 1$ [see Figs. 2(c) and 2(d)] and its suppressed transmittance, $T \gtrsim 0$ [see Figs. 2(e) and 2(f)], as compared to the reflectance, R_0 and transmittance, T_0 of bare graphene [dashed blue lines in Figs. 2(c)–2(f)] [64]. In the high-frequency range, $\omega \gg \omega_{\rm mp}$, the situation is opposite, namely, the wavelength of the incident electromagnetic wave is considerably shorter than the period of the structure, $\lambda \ll D$, and, of course, also smaller than the hole width, $\lambda \ll W$. In this case the metal film almost does not influence the propagation of the electromagnetic wave, hence the reflectance, R, and the transmittance, T, of graphene with perforated metal film almost coincide with those of bare graphene (R_0 and T_0).

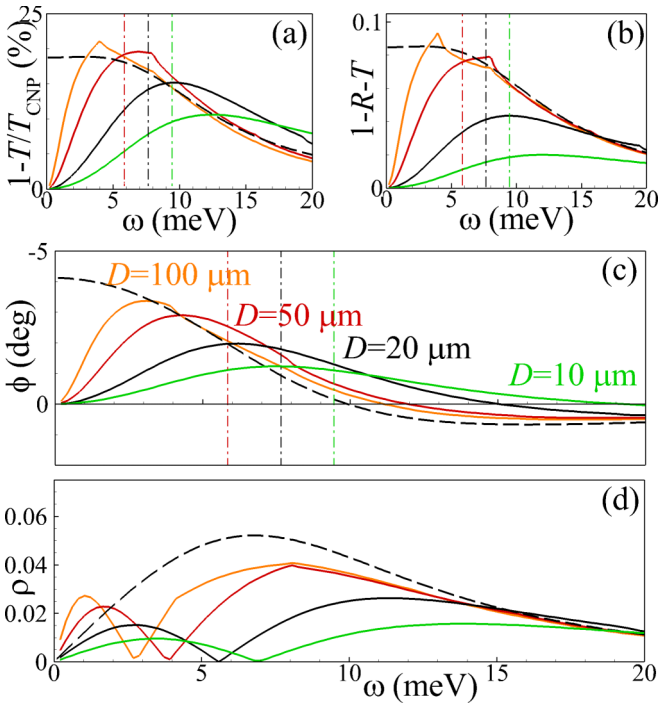

FIG. 3. Frequency dependence of the extinction (a), the absorbance (b), Faraday rotation angle (c), and transmitted wave ellipticity (d) of the doped graphene monolayer placed into the magnetic field with B = 1.5 T and cladded between the semi-infinite Al_2O_3 substrate and metal film with hole grating of period $D = 100\,\mu$m (solid orange lines), $D = 50\,\mu$m (solid red lines), $D = 20\,\mu$m (solid black lines), or $D = 10\,\mu$m (solid green lines). Other parameters are the same as in Fig. 2. In panels (a)–(c), vertical dash-and-dotted lines depict the frequencies of the magnetoplasmon resonance for wave vector $k = 2\pi/D$ with $D = 50\,\mu$m (red lines), $D = 20\,\mu$m (black lines), and $D = 10\,\mu$m (green lines). In all panels the black dashed lines correspond to the extinction $1 - T_0/T_{0,\rm CNP}$, absorbance $1 - R_0 - T_0$, Faraday rotation angle ϕ_0 and ellipticity ρ_0 of the transmitted wave in the case of bare graphene.

The most interesting situation takes place in the intermediate frequency range, when the frequency of the incident wave is close to the magnetoplasmon resonance frequency $\omega \sim \omega_{\rm mp}$. As it can be seen from Figs. 2(e) and 2(f), it is in this frequency range that the maximal deviation between the transmittance of the perforated metal film with doped graphene (T) and that of the same structure with undoped graphene ($T_{\rm CNP}$) takes place owing to the the excitation of magnetoplasmons. In more details this phenomenon is shown in Figs. 3(a) and 4(a). Near the frequency of magnetoplasmon resonance, $\omega_{\rm mp}$ (depicted by vertical dash-and-dotted lines), the extinction attains its local maximum, as does the absorbance, $1 - R - T$ [see Figs. 3(b) and 4(b)]. Interestingly, both the extinction and the absorbance attain their maxima also in the structures that do not allow for the excitation of magnetoplasmons. Such a situation can take place in two kinds of structures:

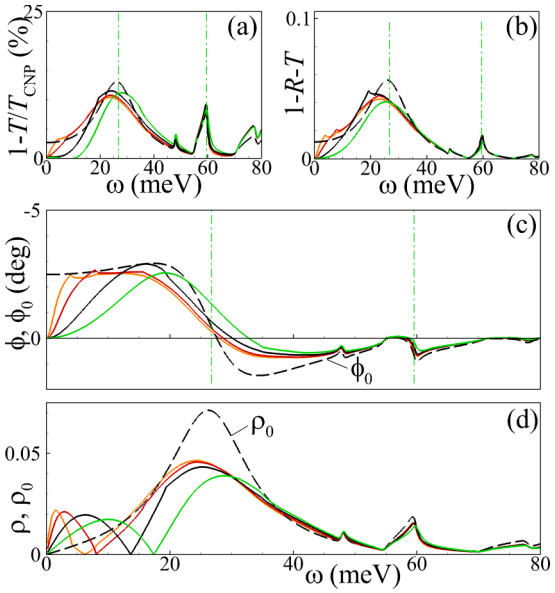

FIG. 4. The same as described in the caption of Fig. 3, but for the magnetic field B = 7 T.

(i) graphene layer without perforated metallic film [dashed black lines in Figs. 3 and 4]; (ii) graphene layer with grating but when the lattice vector of the latter, $g = 2\pi/D$, is below the threshold k_{th} (that is, when the period D is too large, so that the magnetoplasmon resonance eigenfrequency does not exist)—see the corresponding spectra in Figs. 2(a) and 2(b). Examples of such situation can be found for structures with $D = 100\,\mu$m (orange lines) in Figs. 3(a) and 3(b), as well as for $D = 100\,\mu$m (orange lines), $D = 50\,\mu$m (red lines), and $D = 20\,\mu$m (black lines) in Figs. 4(a) and 4(b). Nevertheless, in these cases the extinction and absorbance attain their maxima in the vicinity of the cyclotron frequency ω_c owing to the resonant interaction between the electromagnetic wave and graphene's charge carriers, rotating in the perpendicular magnetic field (in more details this phenomenon will be described in Sec. IV). It should be noticed, that at low magnetic field [Figs. 3(a) and 3(b)] there is a certain discrepancy between the predicted magnetoplasmon resonance and the maxima of absorbance and extinction. The reason for this seems to be the following: the relaxation rate of free carriers in graphene used in the calculation was $\gamma = 7.54$ meV; i.e., its value is comparable with the predicted frequencies of magnetoplasmon resonance ω_{mp}. As a result, the magnetoplasmon oscillations are overdamped in this case. A possible solution of this problem is to shift the magnetoplasmon resonance to the higher-frequency range, e.g., by increasing the external magnetic field strength B. In this case the agreement between the predicted magnetoplasmon resonance frequency and the maxima of the absorbance and the extinction is considerably better [see Figs. 4(a) and 4(b)]. At the same time, the maxima in the extinction and absorbance spectra at $\omega_{\text{mp}} \approx 59.5$ meV appear owing to the excitation of the aforementioned surface phonon polaritons.

How does the excitation of the graphene magnetoplasmons, which manifests itself by the increase of extinction and absorbance, influence the Faraday rotation angle of the transmitted wave? To answer this question we compare the Faraday rotation angle ϕ of the electromagnetic wave transmitted through the perforated metal film on top of the doped graphene layer [solid lines in Figs. 3(c) and 4(c)] with that (ϕ_0) of the electromagnetic wave passing through bare graphene with the same parameters but without the grating [dashed lines in Figs. 3(c) and 4(c)]. The formulas permitting to calculate the Faraday rotation angle from zero-harmonics amplitudes $H^{(t)}_{x||0,0} H^{(t)}_{y||0,0}$ can be found, e.g., in Ref. [65]. It is evident that in the low-frequency region, $\omega \ll \omega_{\text{mp}}$, the rotation angle ϕ is considerably below ϕ_0, i.e., the presence of the perforated metal film hampers the Faraday rotation effect. This fact is a consequence of the above-mentioned attenuated transmittance of the perforated metal film, shown in Figs. 2(c) and 2(d). Notice that the decrease of the Faraday rotation angle, ϕ (compared to ϕ_0), in the low-frequency range is accompanied by the enhancement of the ellipticity, ρ, of the transmitted wave polarization (again, compared to the ellipticity ρ_0 of the polarization of the electromagnetic wave transmitted through the bare graphene)—see Figs. 3(d) and 4(d). In the high-frequency range, where $\omega \gg \omega_{\text{mp}}$, the aforementioned negligible interaction between the electromagnetic wave and perforated metal film [see Figs. 2(c) and 2(d)] reveals into the fact that $\phi \approx \phi_0$ and $\rho \approx \rho_0$. Nevertheless, in the intermediate frequency range, $\omega \sim \omega_{\text{mp}}$, when the magnetoplasmon resonance eigenfrequency does exist [red, black, and green solid lines in Figs. 3(c) and 3(d), as well as green solid lines in Figs. 4(c) and 4(d)], the ellipticity $\rho < \rho_0$ (so, the transmitted wave polarization becomes closer to the linearly polarized wave), but the Faraday rotation angle satisfies the condition $\phi > \phi_0$. In other words, excitation of graphene magnetoplasmons owing to the presence of the perforated metal film on top of graphene increases the Faraday rotation angle. In the situation, where the magnetoplasmon resonance eigenfrequency does not exist [$2\pi/D < k_{\text{th}}$, examples are orange solid lines in Figs. 3(c) and 3(d), as well as orange, red, and black solid lines in Figs. 4(c) and 4(d)] the Faraday rotation angle ϕ is almost the same as ϕ_0 (or even less), even though the ellipticity ρ can be smaller than ρ_0.

More detailed information of how the presence of the perforated metal film on top of graphene changes the Faraday rotation angle can be extracted from Fig. 5, which demonstrates the dependence of the Faraday angle difference, $\Delta\phi = |\phi| - |\phi_0|$, upon the frequency ω and the period of the hole grating D. It is clearly seen that in the intermediate frequency range [4 meV $\lesssim \omega \lesssim$ 12 meV in Fig. 5(a) and 15 meV $\lesssim \omega \lesssim$ 30 meV in Fig. 5(b)] the Faraday angle difference is positive, $\Delta\phi > 0$, that is, the presence of the perforated metal film increases the absolute value of the Faraday rotation angle as compared to the case without the grating. Beyond this frequency range the Faraday angle difference is mainly negative, $\Delta\phi < 0$ [66]. In other words, both in the low- and in the high-frequency ranges presence of the perforated metal film on top of graphene suppresses the Faraday rotation of transmitted wave. At the same time, inside the intermediate frequency range there exist some optimal values of the hole grating period $D \approx 17\,\mu$m [in Fig. 5(a)] and $D \approx 8\,\mu$m [in Fig. 5(b)], for which the Faraday angle difference is maximal and exceeds 1°.

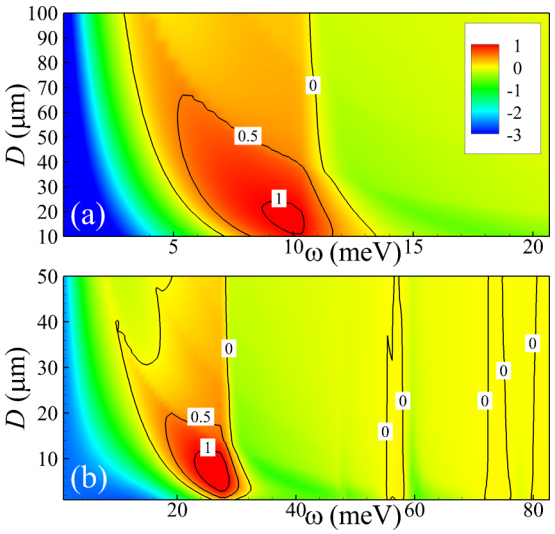

FIG. 5. Faraday rotation angle difference $\Delta\phi$ (in degrees, depicted by color map) versus frequency ω and period of the hole array D for the graphene layer placed into perpendicular magnetic field with $B = 1.5\,T$ (a) or $B = 7\,T$ (b) and cladded by the semi-infinite Al_2O_3 substrate and the metal film with the periodic array of holes, which widths are $W = 0.9\,D$. Other parameters are the same as those described in the caption of Fig. 2.

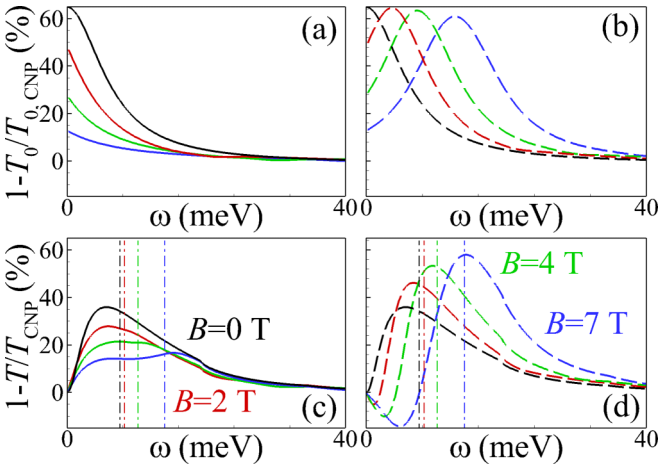

FIG. 6. (a), (b) Frequency dependence of the extinction of the clockwise (a) and counterclockwise (b) circularly polarized electromagnetic wave transmitted through graphene with Fermi energy $\mu = -0.358$ eV and relaxation rate $\gamma = 3.68$ meV on semi-infinite Al_2O_3 substrate, subjected to perpendicular magnetic field of strength $B = 0$ T (black lines), $B = 2$ T (red lines), $B = 4$ T (green lines), and $B = 7$ T (blue lines); (c), (d) The extinction (as a function of frequency) of the clockwise (c) and counterclockwise (d) circularly polarized electromagnetic wave impinging on the graphene cladded by semi-infinite Al_2O_3 substrate and perforated metal film with parameters $D = 20\,\mu$m, $W = 18\,\mu$m, $d = 50$ nm. The parameters of graphene, the magnetic field values, and the meaning of the different curves are the same as those in panels (a) and (b).

IV. MAGNETIC CIRCULAR DICHROISM

The term dichroism means the property shown by certain materials of having different absorption coefficients for light polarized in different directions [65]. If the amplitudes of the transmitted clockwise and counterclockwise polarized waves will not be equal in the presence of a magnetic field applied along their direction of propagation, the material possesses the magnetic circular dichroism (MCD). This is different from the Faraday rotation effect that exists in nonabsorbing media. Applying a magnetic field to the dielectric causes the material to exhibit circular birefringence, i.e., the propagation velocities of the clockwise and counterclockwise polarized waves become unequal. The Faraday rotation angle is then proportional to the difference in the refractive indices for two circular polarizations [67]. Of course, the two effects are interconnected, especially in an intrinsically absorbing plasmonic structure such as the one considered here, but still we can attempt to make a distinction between them. Let us point it out that the system under study has no dichroism in the absence of magnetic field.

To clarify the influence of magnetoplasmons on the MCD of the structure, we consider first the extinction of the clockwise and counterclockwise circularly polarized electromagnetic waves [depicted in Figs. 6(a) and 6(b), respectively], transmitted through the graphene layer without 2D grating on top of it. A clockwise polarized incident wave is characterized by the $\pi/2$ phase shift between the x and y components of its magnetic field ($H_y^{(i)} = i\,H_x^{(i)}$), while their amplitudes are equal. The phase shift between the magnetic field components in the counterclockwise circularly polarized incident wave is $-\pi/2$; i.e., $H_y^{(i)} = -i\,H_x^{(i)}$.

As follows from the comparison of Figs. 6(a) and 6(b), at zero magnetic field (black lines) the extinction values of clockwise and counterclockwise circularly polarized electromagnetic waves are equal. When graphene is doped with holes (negative chemical potential $\mu < 0$), application of external magnetic field results in the MCD: for the same frequency the extinction of the counterclockwise polarized wave [Fig. 6(b)] exceeds that of the clockwise circularly polarized wave [Fig. 6(a)]. The frequency dependence of the extinction, being a monotonically decreasing function in the case of clockwise polarized wave, in the case of counterclockwise polarized wave exhibits its maximum at the cyclotron frequency ω_c. As a consequence, the growth of the magnetic field leads to the blue-shift of the maximum of the counterclockwise polarized wave extinction spectrum [Fig. 6(b)] and to a monotonic decrease of the clockwise polarized wave extinction [see Fig. 6(a)].

Adding the perforated metal film on top of graphene changes considerably the extinction spectrum. Thus, in the low-frequency region both clockwise and counterclockwise circularly polarized waves [depicted in Figs. 6(c) and 6(d), correspondingly] are characterized by diminished extinction owing to the aforementioned long-wavelength screening. This result is completely different from the extinction spectra of the perforated graphene, considered in Ref. [59]: in the low-frequency region perforated graphene exhibits enhanced extinction. Along with this, the extinction values for electromagnetic waves of both polarizations reach their maxima in the vicinity of the magnetoplasmon resonance frequency ω_{mp} [which frequencies are calculated from Eq. (15) and depicted in Figs. 6(c) and 6(d) by vertical dash-and-dotted lines]. For the clockwise polarization [Fig. 6(c)] such a behavior is quite

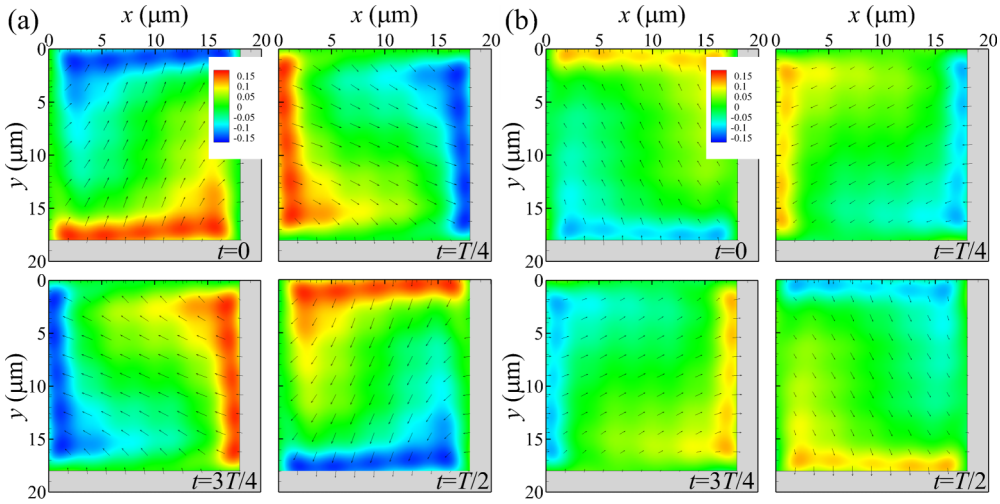

FIG. 7. Spatial distribution (over a unit cell of the periodically perforated metal film) of the electric field components $E_z^{(3)}(\mathbf{r},d/2)$ (depicted by color map) and $E_x^{(3)}(\mathbf{r},d/2)$, $E_y^{(3)}(\mathbf{r},d/2)$ (depicted by vectors) on graphene, subjected to the magnetic field $B = 7\,\mathrm{T}$ for the clockwise [box (a)] and counterclockwise [box (b)] circularly polarized incident waves with frequency $\omega = 14\,\mathrm{meV}$ at time moments $t = 0$ (upper left panels in each box), after quarter-period $t = \pi/2\omega$ (upper right panels), after half-period $t = \pi/2\omega$ (lower right panels), and after three-quarters of the period $t = 3\pi/2\omega$ (lower left panels). Other parameters of the structure are the same as those in Fig. 6.

different from that of bare graphene [where the extinction is a monotonically decreasing function of frequency, see Fig. 6(a)]. It is worth noting that in the case of clockwise polarization the graphene with perforated metal film is characterized by the magnetoplasmon-enhanced extinction. Indeed, in the vicinity of magnetoplasmon resonance frequency the extinction of such structure exceeds that of the graphene without metal film. For the counterclockwise polarization [Fig. 6(d)] the resonant excitation of magnetoplasmons results in the blue-shift of the extinction maximum, compared to the case of bare graphene [Fig. 6(b)]. Noteworthy, in the low-frequency range the counterclockwise polarized wave is characterized by a negative extinction, which becomes more pronounced at high magnetic field [compare red and blue lines in Fig. 6(d), which correspond to $B = 2\,\mathrm{T}$ and $B = 7\,\mathrm{T}$, respectively].

At the same time, the high magnetic field provides a better correspondence between the frequency of maximal extinction and the frequency of the magnetoplasmon resonance for both polarizations. It can be seen from the comparison of black, red, green, and blue solid lines maxima in Figs. 6(c) and 6(d) with the positions of the vertical dash-and-dotted lines of respective colors. Indeed, for $B = 7\,\mathrm{T}$ (blue solid and dash-and-dotted line) the difference is negligible. The respective spatial distributions of the electric field on graphene in the vicinity of the magnetoplasmon resonance frequency are shown in Fig. 7 for clockwise and counterclockwise circularly polarized incident waves [Figs. 7(a) and 7(b), respectively]. For both polarizations, z component of the electric field (depicted by color map) has a maximum and a minimum near the opposite edges of the square hole at the magnetoplasmon resonance. In other words, the distribution of charge carriers in graphene is dipolar. During one period of the electromagnetic wave, $T = 2\pi/\omega$, the dipolar distribution rotates along the hole perimeter in the same direction as the incident wave's polarization vector, clockwise [Fig. 7(a)] or counterclockwise [Fig. 7(b)].

When the graphene is doped with electrons (positive chemical potential, $\mu > 0$, Fig. 8), the extinction of the clockwise polarized wave [Fig. 8(a)] at high-frequency range is larger than that of the counterclockwise polarized wave [Fig. 8(c)]. The situation is totally opposite to the case of graphene doped with holes [compare Figs. 8(a) and 6(c) as well as Figs. 8(c) and 6(d)]. Moreover, if compared to the case of the linearly polarized incident wave with the same parameters [shown in Fig. 3], the one with clockwise circular polarization both exhibit a stronger extinction [compare Figs. 8(a) and 3(a)]

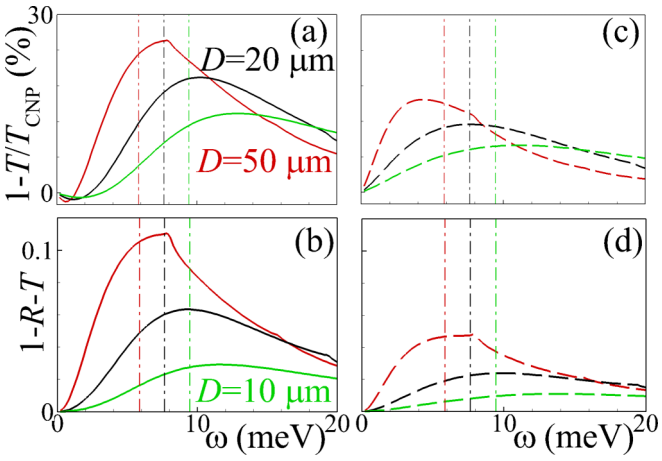

FIG. 8. Frequency dependence of the extinction [upper row, panels (a) and (c)], and absorbance [lower row, panels (b) and (d)] of the clockwise [left column, panels (a) and (b)] and counterclockwise [right column, panels (a) and (b)] circularly polarized electromagnetic wave impinging on graphene cladded by a semi-infinite Al_2O_3 substrate and a perforated metal film (2D grating), subjected to a perpendicular magnetic field. The parameters of the structure and the meaning of the different curves are the same as described in the caption of Fig. 3.

and stronger absorbance [compare Figs. 8(b) and 3(b)]. At the same time, the case of counterclockwise circular polarization is quite different: here the extinction and the absorbance are considerably lower than those of linearly polarized incident wave [compare Figs. 8(c) and 3(a) as well as Figs. 8(d) and 3(b)]. The dependence of the magnetic circular dichroism upon the parameters of the perforated metal film is described in Appendix C.

V. CONCLUSIONS

To conclude, we calculated the spectral dependence of the Faraday rotation and MCD of an electromagnetic wave transmitted through a graphene layer subjected to an external perpendicular magnetic field. The calculations show that these effects are strongly influenced by adding a periodically perforated metallic film (a 2D grating) on top of graphene. We have demonstrated that, if the width of the perforation holes is close to the array period (i.e., the grating looks like a thin metallic net), the incident electromagnetic wave is strongly screened by this structure in the low-frequency range. It results in a decrease of the Faraday rotation angle of the transmitted wave, in comparison with bare graphene. In contrast, if the wave frequency is close to that of the magnetoplasmon resonance supported by the structure with 2D grating, one can expect an increase of the Faraday rotation angle, which is a result of the magnetoplasmon-mediated transmission. The maximum of the Faraday rotation angle is shifted to higher frequency when the period of the grating decreases. An important advantage of the graphene-based structure with 2D grating is that it introduces lower ellipticity to the transmitted linear polarized wave and for some frequencies it can vanish, which means maintaining the linear polarization (see Fig. 3). It can be potentially interesting for making a switchable rotating polariser in the THz range by combining a stack of graphene layers with a thin metal net on top of each of them to get high rotation angles.

The effect introduced by the grating is even more substantial for the MCD, which is quantified by the difference in the extinction between left-hand and right-hand circular polarized waves [68] (Fig. 8). We notice that the dichroism changes its sign depending on the wave frequency and the crossover point in the spectrum can be tuned by adjusting magnetic field and also the graphene Fermi energy that determine the magnetoplasmon dispersion curve. This opens the way to design an electrically switchable optical isolator based on the MCD effect by utilizing nonreciprocal losses [59].

One possible extension of this work can be the study of other (nonsquare) types of hole arrays (e.g., triangular, rectangular, random, etc.), which are nonsymmetric with respect to the polarization plane of the incident wave. Since the condition for the momentum conservation, which is necessary for the excitation of magnetoplasmons, can also be achieved by using nonsquare hole gratings, general phenomena (related to the magnetoplasmon excitation) will be qualitatively the same. Nevertheless, for the nonsymmetric hole arrays the transmittance and the Faraday rotation angle will depend upon the direction of polarization of the incident wave with respect to the translation vectors of the 2D grating. Another possible further development of the present work may consist in taking into account the dependence of the substrate dielectric constant upon the magnetic field, which can result in the additional anisotropy and, as a consequence, in a dependence of the transmittance upon the direction of the external magnetic field. It can also be interesting to consider a thin spacer between the graphene and the metal grating that could work as a resonator and can eventually enhance the magnetoplasmon's amplitude and the effect induced by them in the structure. Also this type of structure allows one to use graphene magnetoplasmons for the controlling of spoof plasmons in the metal grating [69] as well as the enhanced optical transmission [70].

ACKNOWLEDGMENTS

The authors thank Alexey Kuzmenko and Jean-Marie Poumirol from the University of Geneva, Switzerland, and Luis Martín-Moreno from the University of Zaragoza, Spain, for the careful reading and valuable discussions and comments. Funding from the European Commission within the project "Graphene-Driven Revolutions in ICT and Beyond" (Ref. No. 696656) and the Portuguese Foundation for Science and Technology (FCT) in the framework of the Strategic Funding UID/FIS/04650/ 2013 is gratefully acknowledged.

APPENDIX A: EXPLICIT FORM OF THE ELECTROMAGNETIC FIELDS

1. Solutions of Maxwell equations in different media

Assuming electromagnetic field time-dependence as $\mathbf{E},\mathbf{H} \sim \exp(-i\omega t)$, we represent the Maxwell equations as

$$\mathrm{rot}\,\mathbf{E}^{(m)} = \frac{i\omega}{c}\mathbf{H}^{(m)}, \tag{A1}$$

$$\mathrm{rot}\,\mathbf{H}^{(m)} = -\frac{i\omega}{c}\varepsilon_m\mathbf{E}^{(m)}, \tag{A2}$$

$$\mathrm{div}\,\mathbf{E}^{(m)} = 0, \tag{A3}$$

$$\mathrm{div}\,\mathbf{H}^{(m)} = 0, \tag{A4}$$

where ω is the frequency, and c is the velocity of light in vacuum. The superscripts $m = 1,2,3$ correspond to the spatial domains $z < -d/2$, $-d/2 < z < d/2$, and $z > d/2$, respectively. Consequently, the dielectric constants are: $\varepsilon_1 = \varepsilon_2 = 1, \varepsilon_3 = \varepsilon$. After substituting Eq. (A1) into (A2), and using Eq. (A3), one obtains

$$\left[\frac{\partial^2}{\partial x^2} + \frac{\partial^2}{\partial y^2} + \frac{\partial^2}{\partial z^2} + \frac{\omega^2}{c^2}\varepsilon_m\right]\mathbf{E}^{(m)} = 0. \tag{A5}$$

In a similar manner, substitution of Eq. (A2) into (A1) gives [taking into account Eq. (A4)]

$$\left[\frac{\partial^2}{\partial x^2} + \frac{\partial^2}{\partial y^2} + \frac{\partial^2}{\partial z^2} + \frac{\omega^2}{c^2}\varepsilon_m\right]\mathbf{H}^{(m)} = 0. \tag{A6}$$

Inside the holes in the metal film (spatial domain $-d/2 < z < d/2$, $m = 2$), we can consider z components of the electromagnetic field, $E_z^{(2)}$ and $H_z^{(2)}$, as independent

variables, thus

$$\frac{\partial^2 E_z^{(2)}}{\partial x^2}+\frac{\partial^2 E_z^{(2)}}{\partial y^2}+\frac{\partial^2 E_z^{(2)}}{\partial z^2}+\frac{\omega^2}{c^2}E_z^{(2)}=0, \tag{A7}$$

$$\frac{\partial^2 H_z^{(2)}}{\partial x^2}+\frac{\partial^2 H_z^{(2)}}{\partial y^2}+\frac{\partial^2 H_z^{(2)}}{\partial z^2}+\frac{\omega^2}{c^2}H_z^{(2)}=0. \tag{A8}$$

As a result, we can divide eigenfunctions into two types: (i) E-waves with $E_z\neq 0$, $H_z\equiv 0$ and (ii) H-waves with $H_z\neq 0$, $E_z\equiv 0$. For E-waves after matching boundary conditions at the hole edges inside the film $E_z^{(2,E)}(lD,y,z)=E_z^{(2,E)}(lD+W,y,z)=0$, $E_z^{(2,E)}(x,l'D,z)=E_z^{(2,E)}(x,l'D+W,z)=0$, we obtain the solution of Eq. (A7) for the electric field's z component inside the film in the form

$$E_z^{(2,E)}(\mathbf{r},z)=\sum_{m,n=1}^{\infty}\sin\left[\frac{m\pi}{W}(x-lD)\right]\sin\left[\frac{n\pi}{W}(y-l'D)\right]\left\{A_{m,n}^{(s)}\sin\left[\mu_{m,n}\left(z+\frac{d}{2}\right)\right]+A_{m,n}^{(c)}\cos\left[\mu_{m,n}\left(z-\frac{d}{2}\right)\right]\right\}, \tag{A9}$$

where $m,n\geqslant 1$ are the mode indices; $A_{m,n}^{(s)}$ and $A_{m,n}^{(c)}$ are the amplitudes of the respective mode (sin- and cos-like wave, correspondingly), $\mu_{m,n}=\sqrt{(\frac{\omega}{c})^2-(\frac{m\pi}{W})^2-(\frac{n\pi}{W})^2}$. Other components of the E-wave electromagnetic field can be represented as

$$H_x^{(2,E)}(\mathbf{r},z)=-\frac{i\omega}{c}\sum_{m,n=1}^{\infty}\frac{1}{\left(\frac{m\pi}{W}\right)^2+\left(\frac{n\pi}{W}\right)^2}\frac{n\pi}{W}\sin\left[\frac{m\pi}{W}(x-lD)\right]\cos\left[\frac{n\pi}{W}(y-l'D)\right]\left\{A_{m,n}^{(s)}\sin\left[\mu_{m,n}\left(z+\frac{d}{2}\right)\right]\right.$$
$$\left.+A_{m,n}^{(c)}\cos\left[\mu_{m,n}\left(z-\frac{d}{2}\right)\right]\right\}, \tag{A10}$$

$$H_y^{(2,E)}(\mathbf{r},z)=\frac{i\omega}{c}\sum_{m,n=1}^{\infty}\frac{1}{\left(\frac{m\pi}{W}\right)^2+\left(\frac{n\pi}{W}\right)^2}\frac{m\pi}{W}\cos\left[\frac{m\pi}{W}(x-lD)\right]\sin\left[\frac{n\pi}{W}(y-l'D)\right]\left\{A_{m,n}^{(s)}\sin\left[\mu_{m,n}\left(z+\frac{d}{2}\right)\right]\right.$$
$$\left.+A_{m,n}^{(c)}\cos\left[\mu_{m,n}\left(z-\frac{d}{2}\right)\right]\right\}, \tag{A11}$$

$$E_x^{(2,E)}(\mathbf{r},z)=\sum_{m,n=1}^{\infty}\frac{\mu_{m,n}}{\left(\frac{m\pi}{W}\right)^2+\left(\frac{n\pi}{W}\right)^2}\frac{m\pi}{W}\cos\left[\frac{m\pi}{W}(x-lD)\right]\sin\left[\frac{n\pi}{W}(y-l'D)\right]\left\{A_{m,n}^{(s)}\cos\left[\mu_{m,n}\left(z+\frac{d}{2}\right)\right]\right.$$
$$\left.-A_{m,n}^{(c)}\sin\left[\mu_{m,n}\left(z-\frac{d}{2}\right)\right]\right\}, \tag{A12}$$

$$E_y^{(2,E)}(\mathbf{r},z)=\sum_{m,n=1}^{\infty}\frac{\mu_{m,n}}{\left(\frac{m\pi}{W}\right)^2+\left(\frac{n\pi}{W}\right)^2}\frac{n\pi}{W}\sin\left[\frac{m\pi}{W}(x-lD)\right]\cos\left[\frac{n\pi}{W}(y-l'D)\right]\left\{A_{m,n}^{(s)}\cos\left[\mu_{m,n}\left(z+\frac{d}{2}\right)\right]\right.$$
$$\left.-A_{m,n}^{(c)}\sin\left[\mu_{m,n}\left(z-\frac{d}{2}\right)\right]\right\}. \tag{A13}$$

Notice that Eqs. (A12)–(A10) also satisfy other natural boundary conditions: zero tangential component of the electric field and zero normal component of the magnetic field at hole surfaces, $E_x^{(2,E)}(x,l'D,z)=E_x^{(2,E)}(x,l'D+W,z)=0$, $E_y^{(2,E)}(lD,y,z)=E_y^{(2,E)}(lD+W,y,z)=0$, $H_x^{(2,E)}(lD,y,z)=H_x^{(2,E)}(lD+W,y,z)=0$, $H_y^{(2,E)}(x,l'D,z)=H_y^{(2,E)}(x,l'D+W,z)=0$.

For H-wave the solution of Eq. (A8) for the z component of the magnetic field can be represented as

$$H_z^{(2,H)}(\mathbf{r},z)=\sum_{m,n=0}^{\infty}\cos\left[\frac{m\pi}{W}(x-lD)\right]\cos\left[\frac{n\pi}{W}(y-l'D)\right]\left\{B_{m,n}^{(s)}\cos\left[\mu_{m,n}\left(z+\frac{d}{2}\right)\right]-B_{m,n}^{(c)}\sin\left[\mu_{m,n}\left(z-\frac{d}{2}\right)\right]\right\}, \tag{A14}$$

while other components of electromagnetic field are

$$H_x^{(2,H)}(\mathbf{r},z)=\sum_{m=1}^{\infty}\sum_{n=0}^{\infty}\frac{\mu_{m,n}}{\left(\frac{m\pi}{W}\right)^2+\left(\frac{n\pi}{W}\right)^2}\frac{m\pi}{W}\sin\left[\frac{m\pi}{W}(x-lD)\right]\cos\left[\frac{n\pi}{W}(y-l'D)\right]\left\{B_{m,n}^{(s)}\sin\left[\mu_{m,n}\left(z+\frac{d}{2}\right)\right]\right.$$
$$\left.+B_{m,n}^{(c)}\cos\left[\mu_{m,n}\left(z-\frac{d}{2}\right)\right]\right\}, \tag{A15}$$

$$H_y^{(2,H)}(\mathbf{r},z)=\sum_{m=0}^{\infty}\sum_{n=1}^{\infty}\frac{\mu_{m,n}}{\left(\frac{m\pi}{W}\right)^2+\left(\frac{n\pi}{W}\right)^2}\frac{n\pi}{W}\cos\left[\frac{m\pi}{W}(x-lD)\right]\sin\left[\frac{n\pi}{W}(y-l'D)\right]\left\{B_{m,n}^{(s)}\sin\left[\mu_{m,n}\left(z+\frac{d}{2}\right)\right]\right.$$
$$\left.+B_{m,n}^{(c)}\cos\left[\mu_{m,n}\left(z-\frac{d}{2}\right)\right]\right\},\tag{A16}$$

$$E_x^{(2,H)}(\mathbf{r},z)=-\frac{i\omega}{c}\sum_{m=0}^{\infty}\sum_{n=1}^{\infty}\frac{1}{\left(\frac{m\pi}{W}\right)^2+\left(\frac{n\pi}{W}\right)^2}\frac{n\pi}{W}\cos\left[\frac{m\pi}{W}(x-lD)\right]\sin\left[\frac{n\pi}{W}(y-l'D)\right]\left\{B_{m,n}^{(s)}\cos\left[\mu_{m,n}\left(z+\frac{d}{2}\right)\right]\right.$$
$$\left.-B_{m,n}^{(c)}\sin\left[\mu_{m,n}\left(z-\frac{d}{2}\right)\right]\right\},\tag{A17}$$

$$E_y^{(2,H)}(\mathbf{r},z)=\frac{i\omega}{c}\sum_{m=1}^{\infty}\sum_{n=0}^{\infty}\frac{1}{\left(\frac{m\pi}{W}\right)^2+\left(\frac{n\pi}{W}\right)^2}\frac{m\pi}{W}\sin\left[\frac{m\pi}{W}(x-lD)\right]\cos\left[\frac{n\pi}{W}(y-l'D)\right]\left\{B_{m,n}^{(s)}\cos\left[\mu_{m,n}\left(z+\frac{d}{2}\right)\right]\right.$$
$$\left.-B_{m,n}^{(c)}\sin\left[\mu_{m,n}\left(z-\frac{d}{2}\right)\right]\right\}.\tag{A18}$$

Here $B_{m,n}^{(s)}$ and $B_{m,n}^{(c)}$ are the amplitudes of sin- and cos-like waves. It should be emphasized that in the case of H-wave along with modes with nonzero indexes $m,n\geqslant 1$, the existence of modes with one zero and another nonzero index (like $m\neq 0$, $n=0$ or $m=0$, $n\neq 0$) is possible. Notice that Eqs. (A15)–(A18) also satisfy the above-mentioned boundary conditions at hole walls $E_x^{(2,H)}(x,l'D,z)=E_x^{(2,H)}(x,l'D+W,z)=0$, $E_y^{(2,H)}(lD,y,z)=E_y^{(2,H)}(lD+W,y,z)=0$, $H_x^{(2,H)}(lD,y,z)=H_x^{(2,H)}(lD+W,y,z)=0$, $H_y^{(2,H)}(x,l'D,z)=H_y^{(2,H)}(x,l'D+W,z)=0$. At the same time, there is no mode with $m=n=0$ [in the summation in Eq. (A14) this term is implicitly excluded], because in this case it is impossible to satisfy above-mentioned boundary conditions on hole walls. Using Eqs. (A10), (A11), (A15), and (A16), it is possible to obtain Eq. (3), which represent the x and y components of the total magnetic field $H_x^{(2)}(\mathbf{r},z)=H_x^{(2,E)}(\mathbf{r},z)+H_x^{(2,H)}(\mathbf{r},z)$, $H_y^{(2)}(\mathbf{r},z)=H_y^{(2,E)}(\mathbf{r},z)+H_y^{(2,H)}(\mathbf{r},z)$ in the matrix form. Similarly, Eq. (4) for the x and y components of the total electric field $E_x^{(2)}(\mathbf{r},z)=E_x^{(2,H)}(\mathbf{r},z)+E_x^{(2,E)}(\mathbf{r},z)$, $E_y^{(2)}(\mathbf{r},z)=E_y^{(2,H)}(\mathbf{r},z)+E_y^{(2,E)}(\mathbf{r},z)$, written in the matrix form, can be obtained from Eqs.(A12), (A13), (A17), and (A18).

Both inside the semi-infinite air ($z<-d/2$, $m=1$) and the semi-infinite substrate ($z>d/2$, $m=3$), we choose transverse (x and y) components of the magnetic field $H_x^{(1,3)}$, $H_y^{(1,3)}$ as independent variables, thus

$$\left[\frac{\partial^2}{\partial x^2}+\frac{\partial^2}{\partial y^2}+\frac{\partial^2}{\partial z^2}+\frac{\omega^2}{c^2}\varepsilon_m\right]H_x^{(m)}=0,\tag{A19}$$

$$\left[\frac{\partial^2}{\partial x^2}+\frac{\partial^2}{\partial y^2}+\frac{\partial^2}{\partial z^2}+\frac{\omega^2}{c^2}\varepsilon_m\right]H_y^{(m)}=0.\tag{A20}$$

Also, we represent solutions of Helmholtz equations (A19) and (A20) as two-dimensional Fourier series with respect to the harmonics with wave vector in (xy) plane $\mathbf{k}_{s,j}$. As a matter of fact, electromagnetic field in vacuum can be represented as

$$H_x^{(1)}(\mathbf{r},z)=H_x^{(i)}\exp\left[ip_{0,0}^{(1)}(z+d/2)\right]+\sum_{s,j=-\infty}^{\infty}H_{x||s,j}^{(r)}\exp\left[i\mathbf{k}_{s,j}\mathbf{r}-ip_{s,j}^{(1)}(z+d/2)\right],\tag{A21}$$

$$H_y^{(1)}(\mathbf{r},z)=H_y^{(i)}\exp\left[ip_{0,0}^{(1)}(z+T/2)\right]+\sum_{s,j=-\infty}^{\infty}H_{y||s,j}^{(r)}\exp\left[i\mathbf{k}_{s,j}\mathbf{r}-ip_{s,j}^{(1)}(z+d/2)\right],\tag{A22}$$

$$H_z^{(1)}(\mathbf{r},z)=\sum_{s,j=-\infty}^{\infty}\frac{sgH_{x||s,j}^{(r)}+jgH_{y||s,j}^{(r)}}{p_{s,j}^{(1)}}\exp\left[i\mathbf{k}_{s,j}\mathbf{r}-ip_{s,j}^{(1)}(z+d/2)\right],\tag{A23}$$

$$E_x^{(1)}(\mathbf{r},z)=H_y^{(i)}\exp\left[ip_{0,0}^{(1)}(z+d/2)\right]-\frac{c}{\omega}\sum_{s,j=-\infty}^{\infty}\left\{p_{s,j}^{(1)}H_{y||s,j}^{(r)}+jg\frac{sgH_{x||s,j}^{(r)}+jgH_{y||s,j}^{(r)}}{p_{s,j}^{(1)}}\right\}\exp\left[i\mathbf{k}_{s,j}\mathbf{r}-ip_{s,j}^{(1)}(z+d/2)\right],\tag{A24}$$

$$E_y^{(1)}(\mathbf{r},z)=-H_x^{(i)}\exp\left[ip_{0,0}^{(1)}(z+d/2)\right]+\frac{c}{\omega}\sum_{s,j=-\infty}^{\infty}\left\{p_{s,j}^{(1)}H_{x||s,j}^{(r)}+sg\frac{sgH_{x||s,j}^{(r)}+jgH_{y||s,j}^{(r)}}{p_{s,j}^{(1)}}\right\}\exp\left[i\mathbf{k}_{s,j}\mathbf{r}+ip_{s,j}^{(1)}(z-d/2)\right],\tag{A25}$$

$$E_z^{(1)}(\mathbf{r},z)=-\frac{c}{\omega}\sum_{s,j=-\infty}^{\infty}\left\{sgH_{y||s,j}^{(r)}-jgH_{x||s,j}^{(r)}\right\}\exp\left[i\mathbf{k}_{s,j}\mathbf{r}-ip_{s,j}^{(1)}(z+d/2)\right].\tag{A26}$$

At the same time, the electromagnetic field components in the substrate are

$$H_x^{(3)}(\mathbf{r},z) = \sum_{s,j=-\infty}^{\infty} H_{x||s,j}^{(t)} \exp\left[i\mathbf{k}_{s,j}\mathbf{r} + ip_{s,j}^{(3)}(z-d/2)\right], \tag{A27}$$

$$H_y^{(3)}(\mathbf{r},z) = \sum_{s,j=-\infty}^{\infty} H_{y||s,j}^{(t)} \exp\left[i\mathbf{k}_{s,j}\mathbf{r} + ip_{s,j}^{(3)}(z-d/2)\right], \tag{A28}$$

$$H_z^{(3)}(\mathbf{r},z) = -\sum_{s,j=-\infty}^{\infty} \frac{sgH_{x||s,j}^{(t)} + jgH_{y||s,j}^{(t)}}{p_{s,j}^{(3)}} \exp\left[i\mathbf{k}_{s,j}\mathbf{r} + ip_{s,j}^{(3)}(z-d/2)\right], \tag{A29}$$

$$E_x^{(3)}(\mathbf{r},z) = \frac{c}{\omega\varepsilon} \sum_{s,j=-\infty}^{\infty} \left\{ p_{s,j}^{(3)} H_{y||s,j}^{(t)} + jg \frac{sgH_{x||s,j}^{(t)} + jgH_{y||s,j}^{(t)}}{p_{s,j}^{(3)}} \right\} \exp\left[i\mathbf{k}_{s,j}\mathbf{r} + ip_{s,j}^{(3)}(z-d/2)\right], \tag{A30}$$

$$E_y^{(3)}(\mathbf{r},z) = -\frac{c}{\omega\varepsilon} \sum_{s,j=-\infty}^{\infty} \left\{ p_{s,j}^{(3)} H_{x||s,j}^{(t)} + sg \frac{sgH_{x||s,j}^{(t)} + jgH_{y||s,j}^{(t)}}{p_{s,j}^{(3)}} \right\} \exp\left[i\mathbf{k}_{s,j}\mathbf{r} + ip_{s,j}^{(3)}(z-d/2)\right]. \tag{A31}$$

$$E_z^{(3)}(\mathbf{r},z) = -\frac{c}{\omega\varepsilon} \sum_{s,j=-\infty}^{\infty} \left\{ sgH_{y||s,j}^{(t)} - jgH_{x||s,j}^{(t)} \right\} \exp\left[i\mathbf{k}_{s,j}\mathbf{r} + ip_{s,j}^{(3)}(z+d/2)\right]. \tag{A32}$$

Equations (A21), (A22), (A24), and (A25) can be written in the matrix form [see Eq. (1)], while Eqs. (A27), (A28), (A30), and (A31) can be transformed into Eq. (2).

2. Boundary conditions and the equations for the field amplitude

Substitution of expressions for the electromagnetic field in the vacuum above the metal film Eq. (1) and electromagnetic field inside the holes Eqs. (3) and (4) into boundary conditions Eqs. (5) and (6) at $z = -d/2$ results in the following system of equations:

$$\begin{aligned} &\begin{pmatrix} H_x^{(i)} \\ H_y^{(i)} \end{pmatrix} + \sum_{s,j=-\infty}^{\infty} \exp[i\mathbf{k}_{s,j}\mathbf{r}] \begin{pmatrix} H_{x||s,j}^{(r)} \\ H_{y||s,j}^{(r)} \end{pmatrix} \\ &= \sum_{m,n=0}^{\infty} \hat{\mathcal{P}}_{m,n}(x - lD,\, y - l'D)\hat{U}_{m,n} \begin{pmatrix} A_{m,n}^{(c)}\delta_{m,0}'\delta_{0,n}' \\ B_{m,n}^{(c)} \end{pmatrix} \cos(\mu_{m,n}d), \quad \begin{matrix} lD \leqslant x \leqslant lD + W, \\ l'D \leqslant y \leqslant l'D + W, \end{matrix} \end{aligned} \tag{A33}$$

$$\begin{aligned} &i\hat{\sigma}_y \begin{pmatrix} H_x^{(i)} \\ H_y^{(i)} \end{pmatrix} - \sum_{s,j=-\infty}^{\infty} \exp[i\mathbf{k}_{s,j}\mathbf{r}] \hat{\mathcal{Q}}_{s,j}^{(1)} \begin{pmatrix} H_{x||s,j}^{(r)} \\ H_{y||s,j}^{(r)} \end{pmatrix} \\ &= \begin{cases} \sum_{m,n=0}^{\infty} \hat{\mathcal{P}}'_{m,n}(x - lD,\, y - l'D)\hat{U}_{m,n} \begin{pmatrix} B_{m,n}^{(s)} + B_{m,n}^{(c)} \sin(\mu_{m,n}d) \\ [A_{m,n}^{(s)} + A_{m,n}^{(c)} \sin(\mu_{m,n}d)]\delta_{m,0}'\delta_{0,n}' \end{pmatrix}, & \begin{matrix} lD \leqslant x \leqslant lD + W, \\ l'D \leqslant y \leqslant l'D + W, \end{matrix} \\ 0, & \text{otherwise.} \end{cases} \end{aligned} \tag{A34}$$

Boundary conditions across the graphene sheet (at $z = d/2$) imply the continuity of the electric field tangential components and discontinuity of the tangential components of the magnetic field (which is defined by the graphene's conductivity), namely:

$$H_x^{(3)}(\mathbf{r},d/2) - H_x^{(2)}(\mathbf{r},d/2) = (4\pi/c)\left[\Sigma_{yx}E_x^{(3)}(\mathbf{r},d/2) + \Sigma_{yy}E_y^{(3)}(\mathbf{r},d/2)\right], \tag{A35}$$

$$H_y^{(3)}(\mathbf{r},d/2) - H_y^{(2)}(\mathbf{r},d/2) = -(4\pi/c)\left[\Sigma_{xx}E_x^{(3)}(\mathbf{r},d/2) + \Sigma_{xy}E_y^{(3)}(\mathbf{r},d/2)\right], \tag{A36}$$

$$E_x^{(3)}(\mathbf{r},d/2) = E_x^{(2)}(\mathbf{r},d/2), \tag{A37}$$

$$E_y^{(3)}(\mathbf{r},d/2) = E_y^{(2)}(\mathbf{r},d/2), \tag{A38}$$

where

$$\Sigma_{xx} = \Sigma_{yy} = i\frac{2\Sigma_0\hbar^2 v_F^2}{l_B^2} \sum_{m=-\infty}^{\infty} \left[\frac{n_F(E_{|m|+1}) - n_F(E_m)}{E_{|m|+1} - E_m} \left\{ \frac{1}{E_{|m|+1} - E_m - \hbar\omega - i\gamma} + \frac{1}{E_m - E_{|m|+1} - \hbar\omega - i\gamma} \right\} \right.$$

$$\left. + \frac{n_F(E_{-(|m|+1)}) - n_F(E_m)}{E_{-(|m|+1)} - E_m} \left\{ \frac{1}{E_{-(|m|+1)} - E_m - \hbar\omega - i\gamma} + \frac{1}{E_m - E_{-(|m|+1)} - \hbar\omega - i\gamma} \right\} \right] (1 + \delta_{m,0}),$$

$$\Sigma_{xy} = -\Sigma_{yx} = \frac{2\Sigma_0\hbar^2 v_F^2}{\pi l_B^2}\sum_{m=-\infty}^{\infty}\left[\frac{n_F(E_{|m|+1}) - n_F(E_m)}{E_{|m|+1} - E_m}\left\{\frac{1}{E_{|m|+1} - E_m - \hbar\omega - i\gamma} - \frac{1}{E_m - E_{|m|+1} - \hbar\omega - i\gamma}\right\}\right.$$
$$\left. + \frac{n_F(E_{-(|m|+1)}) - n_F(E_m)}{E_{-(|m|+1)} - E_m}\left\{\frac{1}{E_{-(|m|+1)} - E_m - \hbar\omega - i\gamma} - \frac{1}{E_m - E_{-(|m|+1)} - \hbar\omega - i\gamma}\right\}\right](1+\delta_{m,0})$$

are the components of the graphene conductivity tensor in magnetic field,

$$\hat{\Sigma} = \begin{pmatrix}\Sigma_{xx} & \Sigma_{xy}\\ \Sigma_{yx} & \Sigma_{yy}\end{pmatrix}.$$

In the above relations, $E_m = \mathrm{sign}(m)\hbar v_F\sqrt{2|m|}/l_B$ are energy levels of the graphene in external magnetic field, $v_F \approx 10^6$ m/s is the Fermi velocity in graphene, $l_B = (\hbar/eB)^{1/2}$ is the magnetic length, $\Sigma_0 = e^2/4\hbar$ is the so-called ac universal conductivity of graphene,

$$n_F(E) = \left[\exp\left(\frac{E-\mu}{kT}\right) + 1\right]^{-1}$$

is the Fermi-Dirac distribution function, μ is the Fermi energy, and γ is the electron relaxation rate in graphene.

Boundary conditions Eqs. (A35)–(A38) can also be written in the matrix form as

$$\begin{pmatrix}H_x^{(2)}(\mathbf{r},d/2)\\ H_y^{(2)}(\mathbf{r},d/2)\\ E_x^{(2)}(\mathbf{r},d/2)\\ E_y^{(2)}(\mathbf{r},d/2)\end{pmatrix} = \begin{pmatrix}\hat{\mathcal{I}} & \hat{\mathcal{G}}\\ 0 & \hat{\mathcal{I}}\end{pmatrix}\begin{pmatrix}H_x^{(3)}(\mathbf{r},d/2)\\ H_y^{(3)}(\mathbf{r},d/2)\\ E_x^{(3)}(\mathbf{r},d/2)\\ E_y^{(3)}(\mathbf{r},d/2)\end{pmatrix}, \tag{A39}$$

with the 2×2 matrix $\hat{\mathcal{G}} = -i(4\pi/c)\hat{\sigma}_y\hat{\Sigma}$ is defined by Eq. (8). Notice that matrix relation Eq. (A39) defines the boundary condition only at the area of holes in the metal film. If we were to add the requirement of zero tangential components of electric field at surface of metal beyond the hole area, then it is possible to represent boundary conditions Eq. (A39) in general form as

$$\begin{pmatrix}E_x^{(3)}(\mathbf{r},d/2)\\ E_y^{(3)}(\mathbf{r},d/2)\end{pmatrix} = \begin{cases}\begin{pmatrix}E_x^{(2)}(\mathbf{r},d/2)\\ E_y^{(2)}(\mathbf{r},d/2)\end{pmatrix} & lD \leqslant x \leqslant lD+W,\\ 0, & l'D \leqslant y \leqslant l'D+W,\\ & \text{otherwise},\end{cases} \tag{A40}$$

and Eq. (7).

Combining Eqs. (2)–(4) with Eqs. (A40) and (7), it is possible to obtain the following expressions for the electromagnetic field at the metal film surface ($z = d/2$):

$$\sum_{s,j=-\infty}^{\infty}\exp[i\mathbf{k}_{s,j}\mathbf{r}]\left(\hat{\mathcal{I}} + \hat{\mathcal{G}}\hat{\mathcal{Q}}_{s,j}^{(3)}\right)\begin{pmatrix}H_{x||s,j}^{(t)}\\ H_{y||s,j}^{(t)}\end{pmatrix}$$
$$= \sum_{m,n=0}^{\infty}\hat{\mathcal{P}}_{m,n}(x-lD,\, y-l'D)\hat{U}_{m,n}\begin{pmatrix}\left[A_{m,n}^{(s)}\sin(\mu_{m,n}d) + A_{m,n}^{(c)}\right]\delta'_{m,0}\delta'_{0,n}\\ B_{m,n}^{(s)}\sin(\mu_{m,n}d) + B_{m,n}^{(c)}\end{pmatrix}, \quad \begin{matrix}lD \leqslant x \leqslant lD+W,\\ l'D \leqslant y \leqslant l'D+W,\end{matrix}; \tag{A41}$$
$$\sum_{s,j=-\infty}^{\infty}\exp[i\mathbf{k}_{s,j}\mathbf{r}]\hat{\mathcal{Q}}_{s,j}^{(3)}\begin{pmatrix}H_{x||s,j}^{(t)}\\ H_{y||s,j}^{(t)}\end{pmatrix}$$
$$= \begin{cases}\sum_{m,n=0}^{\infty}\hat{\mathcal{P}}'_{m,n}(x-lD,\, y-l'D)\hat{U}_{m,n}\begin{pmatrix}B_{m,n}^{(s)}\\ A_{m,n}^{(s)}\delta'_{m,0}\delta'_{0,n}\end{pmatrix}\cos(\mu_{m,n}d), & \begin{matrix}lD \leqslant x \leqslant lD+W,\\ l'D \leqslant y \leqslant l'D+W,.\end{matrix}\\ 0, & \text{otherwise.}\end{cases} \tag{A42}$$

Multiplying Eqs. (A33) and (A41) by $\hat{\mathcal{P}}_{m',n'}(x-lD,\, y-l'D)$ integrating over the area of the hole ($lD \leqslant x \leqslant lD+W$, $l'D \leqslant y \leqslant l'D+W$), and using the orthogonality of trigonometric functions for $m,m',n,n' \geqslant 0$,

$$\int_0^W \sin\left(\frac{m\pi}{W}\xi\right)\sin\left(\frac{m'\pi}{W}\xi\right)d\xi = \frac{W}{2}\delta_{m,m'}\delta'_{m',0},$$
$$\int_0^W \cos\left(\frac{n\pi}{W}\xi\right)\cos\left(\frac{n'\pi}{W}\xi\right)d\xi = \frac{W}{2}(1+\delta_{n',0})\delta_{n,n'},$$

it is possible to obtain equations for the amplitudes Eqs. (9) and (10).

Similarly, multiplying Eqs. (A34) and (A42) by $\exp[-i\mathbf{k}_{s',j'}\mathbf{r}]$, integrating over the area of one period of the structure $lD \leqslant x \leqslant (l+1)D$, $l'D \leqslant y \leqslant (l'+1)D$, and after taking into account orthogonality of the plane waves in the unit cell,

$$\int_0^D dx \int_0^D dy \exp[i(\mathbf{k}_{s,j} - \mathbf{k}_{s',j'})\mathbf{r}] = D^2 \delta_{s,s'} \delta_{j,j'},$$

one can obtain Eqs. (11) and (12).

3. Reflectance and transmittance

To calculate the reflectance and transmittance we notice that the flux density of energy is described by the Poynting vector $\mathbf{S} = (c/8\pi)\mathrm{Re}(\mathbf{E} \times \overline{\mathbf{H}})$. Respectively, using Eqs. (A30) and (A31), the z component of the Poynting vector of the (s,j) harmonics in the substrate can be represented as

$$S^{(t)}_{z||s,j} = \frac{c^2}{8\pi\omega}\mathrm{Re}\left\{ \frac{\overline{H^{(t)}_{y||s,j}}}{\varepsilon}\left[p^{(3)}_{s,j} H^{(t)}_{y||s,j} + jg\frac{sgH^{(t)}_{x||s,j} + jgH^{(t)}_{y||s,j}}{p^{(3)}_{s,j}} \right] + \frac{\overline{H^{(t)}_{x||s,j}}}{\varepsilon}\left[p^{(3)}_{s,j} H^{(t)}_{x||s,j} + sg\frac{sgH^{(t)}_{x||s,j} + jgH^{(t)}_{y||s,j}}{p^{(3)}_{s,j}} \right] \right\}. \tag{A43}$$

In the matrix form this relation can be represented as

$$S^{(t)}_{z||s,j} = \frac{c}{8\pi}\mathrm{Re}\left\{ \left(\overline{H^{(t)}_{y||s,j}}, -\overline{H^{(t)}_{x||s,j}}\right)\hat{\mathcal{Q}}^{(3)}_{s,j}\begin{pmatrix} H^{(t)}_{x||s,j} \\ H^{(t)}_{y||s,j}\end{pmatrix}\right\} = -\frac{c}{8\pi}\mathrm{Re}\left\{ \begin{pmatrix} H^{(t)}_{x||s,j} \\ H^{(t)}_{y||s,j}\end{pmatrix}^{\dagger} i\hat{\sigma}_y \hat{\mathcal{Q}}^{(3)}_{s,j}\begin{pmatrix} H^{(t)}_{x||s,j} \\ H^{(t)}_{y||s,j}\end{pmatrix}\right\}. \tag{A44}$$

In the air, the z component of the Poynting vector of the reflected wave's (s,j) harmonic [using Eqs. (A24) and (A25)] is written as

$$S^{(r)}_{z||s,j} = -\frac{c^2}{8\pi\omega}\mathrm{Re}\left\{ \overline{H^{(r)}_{y||s,j}}\left[p^{(1)}_{s,j} H^{(r)}_{y||s,j} + jg\frac{sgH^{(r)}_{x||s,j} + jgH^{(r)}_{y||s,j}}{p^{(1)}_{s,j}} \right] + \overline{H^{(r)}_{x||s,j}}\left[p^{(1)}_{s,j} H^{(r)}_{x||s,j} + sg\frac{sgH^{(r)}_{x||s,j} + jgH^{(r)}_{y||s,j}}{p^{(1)}_{s,j}} \right] \right\}$$

$$= \frac{c}{8\pi}\mathrm{Re}\left\{ \begin{pmatrix} H^{(r)}_{x||s,j} \\ H^{(r)}_{y||s,j}\end{pmatrix}^{\dagger} i\hat{\sigma}_y \hat{\mathcal{Q}}^{(1)}_{s,j}\begin{pmatrix} H^{(r)}_{x||s,j} \\ H^{(r)}_{y||s,j}\end{pmatrix}\right\}. \tag{A45}$$

The difference of sign in Eqs. (A43) and (A45) reflects the fact that the energy flux of the transmitted wave [see Eq. (A43)] flows in the positive direction of z axis, while that of reflected wave [see Eq. (A45)] flows in the negative direction of z axis. Using the same formalism for the incident wave, we obtain the z component of its Poynting vector in the form

$$S^{(i)}_z = \frac{c}{8\pi}\left[\left|H^{(i)}_x\right|^2 + \left|H^{(i)}_y\right|^2\right]. \tag{A46}$$

The reflectance, R, and the transmittance, T, are defined in the usual way:

$$R = -\frac{\sum_{s,j=-\infty}^{\infty} S^{(r)}_{z||s,j}}{S^{(i)}_z}, \tag{A47}$$

$$T = \frac{\sum_{s,j=-\infty}^{\infty} S^{(t)}_{z||s,j}}{S^{(i)}_z}. \tag{A48}$$

Substituting Eqs. (A44)–(A46) into Eqs. (A47) and (A48), one obtains the expressions for the reflectance and transmittance in the final form of Eqs. (13) and (14).

APPENDIX B: TRANSMITTANCE OF THE GRAPHENE LAYER WITHOUT PERIODICAL STRUCTURE AND THE DISPERSION RELATION OF MAGNETOPLASMONS

When the metal film is absent ($d = 0$), then the right-hand sides of Eqs. (A33) and (A41) become equal [as well as those of Eqs. (A34) and (A42)]. As a consequence, the equality of the left-hand sides of Eqs. (A33) and (A41) [jointly with the equality of left-hand sides of Eqs.(A34) and (A42)] gives

$$\begin{pmatrix} H^{(i)}_x \\ H^{(i)}_y\end{pmatrix} + \sum_{s,j=-\infty}^{\infty} \exp[i\mathbf{k}_{s,j}\mathbf{r}]\begin{pmatrix} H^{(r)}_{x||s,j} \\ H^{(r)}_{y||s,j}\end{pmatrix} = \sum_{s,j=-\infty}^{\infty} \exp[i\mathbf{k}_{s,j}\mathbf{r}](\hat{\mathcal{I}} + \hat{\mathcal{G}}\hat{\mathcal{Q}}^{(3)}_{s,j})\begin{pmatrix} H^{(t)}_{x||s,j} \\ H^{(t)}_{y||s,j}\end{pmatrix}, \tag{B1}$$

$$i\hat{\sigma}_y\begin{pmatrix} H^{(i)}_x \\ H^{(i)}_y\end{pmatrix} - \sum_{s,j=-\infty}^{\infty} \exp[i\mathbf{k}_{s,j}\mathbf{r}]\hat{\mathcal{Q}}^{(1)}_{s,j}\begin{pmatrix} H^{(r)}_{x||s,j} \\ H^{(r)}_{y||s,j}\end{pmatrix} = \sum_{s,j=-\infty}^{\infty} \hat{\mathcal{Q}}^{(3)}_{s,j}\begin{pmatrix} H^{(t)}_{x||s,j} \\ H^{(t)}_{y||s,j}\end{pmatrix}\exp[i\mathbf{k}_{s,j}\mathbf{r}]. \tag{B2}$$

As in Sec. II, we multiply Eqs. (B1) and (B2) by $\exp[-i\mathbf{k}_{s',j'}\mathbf{r}]$ and integrate over the area of one period of the structure $lD \leqslant x \leqslant (l+1)D$, $l'D \leqslant y \leqslant (l'+1)D$. We obtain

$$\begin{pmatrix} H_x^{(i)} \\ H_y^{(i)} \end{pmatrix}\delta_{s',0}\delta_{0,j'} + \begin{pmatrix} H_{x||s',j'}^{(r)} \\ H_{y||s',j'}^{(r)} \end{pmatrix} = \left(\hat{\mathcal{I}} + \hat{\mathcal{G}}\hat{\mathcal{Q}}_{s',j'}^{(3)}\right)\begin{pmatrix} H_{x||s',j'}^{(t)} \\ H_{y||s',j'}^{(t)} \end{pmatrix}, \tag{B3}$$

$$i\hat{\sigma}_y\begin{pmatrix} H_x^{(i)} \\ H_y^{(i)} \end{pmatrix}\delta_{s',0}\delta_{0,j'} - \hat{\mathcal{Q}}_{s',j'}^{(1)}\begin{pmatrix} H_{x||s',j'}^{(r)} \\ H_{y||s',j'}^{(r)} \end{pmatrix} = \hat{\mathcal{Q}}_{s',j'}^{(3)}\begin{pmatrix} H_{x||s',j'}^{(t)} \\ H_{y||s',j'}^{(t)} \end{pmatrix}. \tag{B4}$$

1. Dispersion relation of magnetoplasmons

When $s' \neq 0$ or $j' \neq 0$, Eqs. (B3) and (B4) take the form

$$\begin{pmatrix} H_{x||s',j'}^{(r)} \\ H_{y||s',j'}^{(r)} \end{pmatrix} = \left(\hat{\mathcal{I}} + \hat{\mathcal{G}}\hat{\mathcal{Q}}_{s',j'}^{(3)}\right)\begin{pmatrix} H_{x||s',j'}^{(t)} \\ H_{y||s',j'}^{(t)} \end{pmatrix}, \tag{B5}$$

$$-\hat{\mathcal{Q}}_{s',j'}^{(1)}\begin{pmatrix} H_{x||s',j'}^{(r)} \\ H_{y||s',j'}^{(r)} \end{pmatrix} = \hat{\mathcal{Q}}_{s',j'}^{(3)}\begin{pmatrix} H_{x||s',j'}^{(t)} \\ H_{y||s',j'}^{(t)} \end{pmatrix}. \tag{B6}$$

As a result, the amplitudes of the magnetic field components corresponding to the transmitted wave are governed by the equation

$$\left[\hat{\mathcal{I}} + \left\{\hat{\mathcal{G}} + \left(\hat{\mathcal{Q}}_{s',j'}^{(1)}\right)^{-1}\right\}\hat{\mathcal{Q}}_{s',j'}^{(3)}\right]\begin{pmatrix} H_{x||s',j'}^{(t)} \\ H_{y||s',j'}^{(t)} \end{pmatrix} = 0, \tag{B7}$$

with

$$\left(\hat{\mathcal{Q}}_{s',j'}^{(1)}\right)^{-1} = \begin{pmatrix} -\frac{c}{\omega}\frac{s'j'g^2}{p_{s',j'}^{(1)}} & -\frac{c}{\omega}\frac{(p_{s',0}^{(1)})^2}{p_{s',j'}^{(1)}} \\ \frac{c}{\omega}\frac{(p_{0,j'}^{(1)})^2}{p_{s',j'}^{(1)}} & \frac{c}{\omega}\frac{s'j'g^2}{p_{s',j'}^{(1)}} \end{pmatrix}$$

being the inverse of the matrix $\hat{\mathcal{Q}}_{s',j'}^{(1)}$. If we project $H_{x||s',j'}^{(t)}$, $H_{y||s',j'}^{(t)}$ on the direction of the wave vector $\mathbf{k}_{s',j'} = (s'g, j'g)$, we have

$$\begin{pmatrix} H_{s',j'}^{(\parallel)} \\ H_{s',j'}^{(\perp)} \end{pmatrix} = \hat{\mathcal{V}}_{s',j'}\begin{pmatrix} H_{x||s',j'}^{(t)} \\ H_{y||s',j'}^{(t)} \end{pmatrix},$$

where

$$\hat{\mathcal{V}}_{s',j'} = \frac{1}{\sqrt{s'^2 + j'^2}}\begin{pmatrix} s' & j' \\ -j' & s' \end{pmatrix}$$

is the transformation matrix, $H_{s',j'}^{(\parallel)}$ and $H_{s',j'}^{(\perp)}$ are the components of the magnetic field in the substrate, parallel and perpendicular to the harmonic wave vector $\mathbf{k}_{s',j'}$. In this case, Eq. (B7) can be rewritten as

$$\hat{\mathcal{Z}}_{s',j'}\begin{pmatrix} H_{s',j'}^{(\parallel)} \\ H_{s',j'}^{(\perp)} \end{pmatrix} = 0, \tag{B8}$$

and the matrix

$$\hat{\mathcal{Z}}_{s',j'} = \hat{\mathcal{V}}_{s',j'}\left[\hat{I} + \left\{\hat{\mathcal{G}} + \left(\hat{\mathcal{Q}}_{s',j'}^{(1)}\right)^{-1}\right\}\hat{\mathcal{Q}}_{s',j'}^{(3)}\right](\hat{\mathcal{V}}_{s',j'})^{-1}$$

after some algebra will have the form

$$\hat{\mathcal{Z}}_{s',j'} = \begin{pmatrix} 1 + \frac{4\pi\omega}{c^2}\Sigma_{xx}\frac{1}{p_{s',j'}^{(3)}} + \frac{p_{s',j'}^{(1)}}{p_{s',j'}^{(3)}} & \frac{4\pi}{\omega\varepsilon}\Sigma_{xy}p_{s',j'}^{(3)} \\ -\frac{4\pi\omega}{c^2}\Sigma_{xy}\frac{1}{p_{s',j'}^{(3)}} & 1 + \frac{p_{s',j'}^{(3)}}{\varepsilon p_{s',j'}^{(1)}} + \frac{4\pi}{\omega\varepsilon}\Sigma_{xx}p_{s',j'}^{(3)} \end{pmatrix}.$$

Here we took into account that $\Sigma_{yy} = \Sigma_{xx}$, $\Sigma_{yx} = -\Sigma_{xy}$. Equation (B8) possesses a solution, only when the determinant of matrix $\hat{\mathcal{Z}}_{s',j'}$ is equal to zero. Thus, the magnetoplasmon dispersion relation is

$$\det|\hat{\mathcal{Z}}_{s',j'}| = \left[p_{s',j'}^{(3)} + \frac{4\pi\omega}{c^2}\Sigma_{xx} + p_{s',j'}^{(1)}\right]\left[\frac{\varepsilon}{p_{s',j'}^{(3)}} + \frac{1}{p_{s',j'}^{(1)}} + \frac{4\pi}{\omega}\Sigma_{xx}\right] + \left(\frac{4\pi}{c}\Sigma_{xy}\right)^2 = 0,$$

which after the formal substitution $\mathbf{k}_{s',j'} = \mathbf{k} = (k_x, k_y)$ can be transformed into Eq. (15).

2. The transmittance and the reflectance of the graphene layer on substrate

When $s' = j' = 0$, Eqs. (B3) and (B4) have the form

$$\begin{pmatrix} H_x^{(i)} \\ H_y^{(i)} \end{pmatrix} + \begin{pmatrix} H_{x||0,0}^{(r)} \\ H_{y||0,0}^{(r)} \end{pmatrix} = (\hat{\mathcal{I}} + \hat{\mathcal{G}}\hat{\mathcal{Q}}_{0,0}^{(3)}) \begin{pmatrix} H_{x||0,0}^{(t)} \\ H_{y||0,0}^{(t)} \end{pmatrix}, \tag{B9}$$

$$i\hat{\sigma}_y \begin{pmatrix} H_x^{(i)} \\ H_y^{(i)} \end{pmatrix} - \hat{\mathcal{Q}}_{0,0}^{(1)} \begin{pmatrix} H_{x||0,0}^{(r)} \\ H_{y||0,0}^{(r)} \end{pmatrix} = \hat{\mathcal{Q}}_{0,0}^{(3)} \begin{pmatrix} H_{x||0,0}^{(t)} \\ H_{y||0,0}^{(t)} \end{pmatrix}. \tag{B10}$$

Taking into account that $p_{0,0}^{(1)} = (\omega/c)$, $p_{0,0}^{(3)} = (\omega/c)\sqrt{\varepsilon}$, matrices $\hat{\mathcal{Q}}_{0,0}^{(1)}$ $\hat{\mathcal{Q}}_{0,0}^{(3)}$ can be represented in the simple form

$$\hat{\mathcal{Q}}_{0,0}^{(3)} = \sqrt{\frac{1}{\varepsilon}} i\hat{\sigma}_y, \quad \hat{\mathcal{Q}}_{0,0}^{(1)} = i\hat{\sigma}_y, \tag{B11}$$

and Eqs. (B9) and (B10) can be rewritten as

$$\begin{pmatrix} H_x^{(i)} \\ H_y^{(i)} \end{pmatrix} + \begin{pmatrix} H_{x||0,0}^{(r)} \\ H_{y||0,0}^{(r)} \end{pmatrix} = \left(\hat{\mathcal{I}} + \sqrt{\frac{1}{\varepsilon}}\hat{\mathcal{G}} i\hat{\sigma}_y\right) \begin{pmatrix} H_{x||0,0}^{(t)} \\ H_{y||0,0}^{(t)} \end{pmatrix}, \tag{B12}$$

$$i\hat{\sigma}_y \begin{pmatrix} H_x^{(i)} \\ H_y^{(i)} \end{pmatrix} - i\hat{\sigma}_y \begin{pmatrix} H_{x||0,0}^{(r)} \\ H_{y||0,0}^{(r)} \end{pmatrix} = \sqrt{\frac{1}{\varepsilon}} i\hat{\sigma}_y \begin{pmatrix} H_{x||0,0}^{(t)} \\ H_{y||0,0}^{(t)} \end{pmatrix}. \tag{B13}$$

Multiplying Eq. (B13) by $-i\hat{\sigma}_y$ and summing with Eq. (B12), we obtain

$$2\begin{pmatrix} H_x^{(i)} \\ H_y^{(i)} \end{pmatrix} = \hat{\mathcal{F}} \begin{pmatrix} H_{x||0,0}^{(t)} \\ H_{y||0,0}^{(t)} \end{pmatrix}, \tag{B14}$$

where the matrix

$$\hat{\mathcal{F}} = \left(1 + \sqrt{\frac{1}{\varepsilon}}\right)\hat{\mathcal{I}} + \sqrt{\frac{1}{\varepsilon}}\hat{\mathcal{G}} i\hat{\sigma}_y = \begin{pmatrix} 1 + \frac{4\pi}{c\sqrt{\varepsilon}}\Sigma_{xx} + \sqrt{\frac{1}{\varepsilon}} & \frac{4\pi}{c\sqrt{\varepsilon}}\Sigma_{xy} \\ -\frac{4\pi}{c\sqrt{\varepsilon}}\Sigma_{xy} & 1 + \frac{4\pi}{c\sqrt{\varepsilon}}\Sigma_{xx} + \sqrt{\frac{1}{\varepsilon}} \end{pmatrix},$$

and we took into account that $\Sigma_{yy} = \Sigma_{xx}$, $\Sigma_{yx} = -\Sigma_{xy}$. As a result, the solution of Eq. (B14) can be represented as

$$H_{x||0,0}^{(t)} = 2\sqrt{\varepsilon}\frac{\left(\sqrt{\varepsilon} + \frac{4\pi}{c}\Sigma_{xx} + 1\right)H_x^{(i)} - \frac{4\pi}{c}\Sigma_{xy}H_y^{(i)}}{\left(\sqrt{\varepsilon} + \frac{4\pi}{c}\Sigma_{xx} + 1\right)^2 + \left(\frac{4\pi}{c}\Sigma_{xy}\right)^2}, \tag{B15}$$

$$H_{y||0,0}^{(t)} = 2\sqrt{\varepsilon}\frac{\frac{4\pi}{c}\Sigma_{xy}H_x^{(i)} + \left(\sqrt{\varepsilon} + \frac{4\pi}{c}\Sigma_{xx} + 1\right)H_y^{(i)}}{\left(\sqrt{\varepsilon} + \frac{4\pi}{c}\Sigma_{xx} + 1\right)^2 + \left(\frac{4\pi}{c}\Sigma_{xy}\right)^2}. \tag{B16}$$

Similarly, combining Eqs. (B14) and (B13), one can obtain the expression for the amplitude of the reflected wave magnetic field:

$$\begin{pmatrix} H_{x||0,0}^{(r)} \\ H_{y||0,0}^{(r)} \end{pmatrix} = \left[\hat{\mathcal{I}} - 2\sqrt{\frac{1}{\varepsilon}}\hat{\mathcal{F}}^{-1}\right] \begin{pmatrix} H_x^{(i)} \\ H_y^{(i)} \end{pmatrix},$$

or, equivalently,

$$H_{x||0,0}^{(r)} = \frac{\left(\sqrt{\varepsilon} + \frac{4\pi}{c}\Sigma_{xx}\right)^2 - 1 + \left(\frac{4\pi}{c}\Sigma_{xy}\right)^2}{\left(\sqrt{\varepsilon} + \frac{4\pi}{c}\Sigma_{xx} + 1\right)^2 + \left(\frac{4\pi}{c}\Sigma_{xy}\right)^2}H_x^{(i)} + \frac{\frac{8\pi}{c}\Sigma_{xy}}{\left(\sqrt{\varepsilon} + \frac{4\pi}{c}\Sigma_{xx} + 1\right)^2 + \left(\frac{4\pi}{c}\Sigma_{xy}\right)^2}H_y^{(i)}, \tag{B17}$$

$$H_{y||0,0}^{(r)} = -\frac{\frac{8\pi}{c}\Sigma_{xy}}{\left(\sqrt{\varepsilon} + \frac{4\pi}{c}\Sigma_{xx} + 1\right)^2 + \left(\frac{4\pi}{c}\Sigma_{xy}\right)^2}H_x^{(i)} + \frac{\left(\sqrt{\varepsilon} + \frac{4\pi}{c}\Sigma_{xx}\right)^2 - 1 + \left(\frac{4\pi}{c}\Sigma_{xy}\right)^2}{\left(\sqrt{\varepsilon} + \frac{4\pi}{c}\Sigma_{xx} + 1\right)^2 + \left(\frac{4\pi}{c}\Sigma_{xy}\right)^2}H_y^{(i)}. \tag{B18}$$

Taking into account the particular form of the matrices $\hat{\mathcal{Q}}_{0,0}^{(3)}$ and $\hat{\mathcal{Q}}_{0,0}^{(1)}$ [see Eq. (B11)], the expressions Eqs. (A44) and (A45) for transmitted and reflected wave energy flux density in z direction are written as

$$S_{z||0,0}^{(t)} = \frac{c}{8\pi}\mathrm{Re}\left\{\frac{1}{\sqrt{\varepsilon}}\begin{pmatrix} H_{x||0,0}^{(t)} \\ H_{y||0,0}^{(t)} \end{pmatrix}^{\dagger}\begin{pmatrix} H_{x||0,0}^{(t)} \\ H_{y||0,0}^{(t)} \end{pmatrix}\right\}, \quad S_{z||0,0}^{(r)} = -\frac{c}{8\pi}\mathrm{Re}\left\{\begin{pmatrix} H_{x||0,0}^{(r)} \\ H_{y||0,0}^{(r)} \end{pmatrix}^{\dagger}\begin{pmatrix} H_{x||0,0}^{(r)} \\ H_{y||0,0}^{(r)} \end{pmatrix}\right\}.$$

Accordingly, from Eqs. (A47) and (A48), the transmittance and reflectance can be expressed as

$$T_0 = \frac{\mathrm{Re}\left\{\sqrt{\frac{1}{\varepsilon}}\left(\left|H^{(t)}_{x||0,0}\right|^2 + \left|H^{(t)}_{y||0,0}\right|^2\right)\right\}}{\left|H^{(i)}_x\right|^2 + \left|H^{(i)}_y\right|^2}, \tag{B19}$$

$$R_0 = \frac{\left|H^{(r)}_{x||0,0}\right|^2 + \left|H^{(r)}_{y||0,0}\right|^2}{\left|H^{(i)}_x\right|^2 + \left|H^{(i)}_y\right|^2}. \tag{B20}$$

Finally, after substituting the expressions for the magnetic field components Eqs. (B15)–(B18) into Eqs. (B19) and (B20), one can obtain the transmittance and the reflectance of bare graphene in the following form:

$$T_0 = \frac{4\mathrm{Re}\left(\sqrt{\frac{1}{\varepsilon}}\right)}{\left|H^{(i)}_x\right|^2 + \left|H^{(i)}_y\right|^2}\left\{\left|\sqrt{\varepsilon}\frac{\left(\sqrt{\varepsilon}+\frac{4\pi}{c}\Sigma_{xx}+1\right)H^{(i)}_x - \frac{4\pi}{c}\Sigma_{xy}H^{(i)}_y}{\left(\sqrt{\varepsilon}+\frac{4\pi}{c}\Sigma_{xx}+1\right)^2+\left(\frac{4\pi}{c}\Sigma_{xy}\right)^2}\right|^2 + \left|\sqrt{\varepsilon}\frac{\frac{4\pi}{c}\Sigma_{xy}H^{(i)}_x + \left(\sqrt{\varepsilon}+\frac{4\pi}{c}\Sigma_{xx}+1\right)H^{(i)}_y}{\left(\sqrt{\varepsilon}+\frac{4\pi}{c}\Sigma_{xx}+1\right)^2+\left(\frac{4\pi}{c}\Sigma_{xy}\right)^2}\right|^2\right\}, \tag{B21}$$

$$R_0 = \frac{1}{\left|H^{(i)}_x\right|^2 + \left|H^{(i)}_y\right|^2}\left\{\left|\frac{\left(\sqrt{\varepsilon}+\frac{4\pi}{c}\Sigma_{xx}\right)^2 - 1 + \left(\frac{4\pi}{c}\Sigma_{xy}\right)^2}{\left(\sqrt{\varepsilon}+\frac{4\pi}{c}\Sigma_{xx}+1\right)^2+\left(\frac{4\pi}{c}\Sigma_{xy}\right)^2}H^{(i)}_x + \frac{\frac{8\pi}{c}\Sigma_{xy}}{\left(\sqrt{\varepsilon}+\frac{4\pi}{c}\Sigma_{xx}+1\right)^2+\left(\frac{4\pi}{c}\Sigma_{xy}\right)^2}H^{(i)}_y\right|^2\right.$$
$$\left. + \left|\frac{\frac{8\pi}{c}\Sigma_{xy}}{\left(\sqrt{\varepsilon}+\frac{4\pi}{c}\Sigma_{xx}+1\right)^2+\left(\frac{4\pi}{c}\Sigma_{xy}\right)^2}H^{(i)}_x - \frac{\left(\sqrt{\varepsilon}+\frac{4\pi}{c}\Sigma_{xx}\right)^2 - 1 + \left(\frac{4\pi}{c}\Sigma_{xy}\right)^2}{\left(\sqrt{\varepsilon}+\frac{4\pi}{c}\Sigma_{xx}+1\right)^2+\left(\frac{4\pi}{c}\Sigma_{xy}\right)^2}H^{(i)}_y\right|^2\right\}. \tag{B22}$$

APPENDIX C: COEFFICIENT OF MAGNETIC CIRCULAR DICHROISM

To characterize quantitatively the circular dichroism in our magnetoactive graphene-based structure, we introduce the coefficient of circular dichroism,

$$\tau = \frac{T_a - T_c}{T_a + T_c},$$

which is expressed in terms of the transmittance of the clockwise and counterclockwise circularly polarized waves T_c and T_a. The dependence of the coefficient of the circular dichroism upon the frequency ω and the period of the hole array D is shown in Fig. 9. It can be seen that the coefficient of the optical dichroism τ achieves its maximum in the vicinity of $\omega \approx 8$ meV [for weak magnetic field, see Fig. 9(a)] or $\omega \approx 25$ meV [for strong magnetic field, see Fig. 9(b)]. The maximal value of the optical dichoism coefficient grows monotonically with the increase of the hole array period D. Notice that the coefficient of optical dichroism of the perforated metal film deposited on top of graphene monolayer τ is always smaller than that of bare graphene, τ_0 [compare dashed and solid lines in upper plots in Figs. 9(a) and 9(b)]. In other words, the presence of the perforated metallic film on top of the graphene sheet reduces the relative contrast between the transmittances of clockwise and counterclockwise polarized waves. The physical reason for this is the diffraction of the incident electromagnetic wave on the graphene with periodic structure, which gives rise to the partial conversion of the incident wave energy into the energy of the excited magnetoplasmons, thus reducing the transmittance of this structure for both circular polarizations (clockwise and counterclockwise). However, the stronger decrease of the counterclockwise circularly polarized wave transmittance

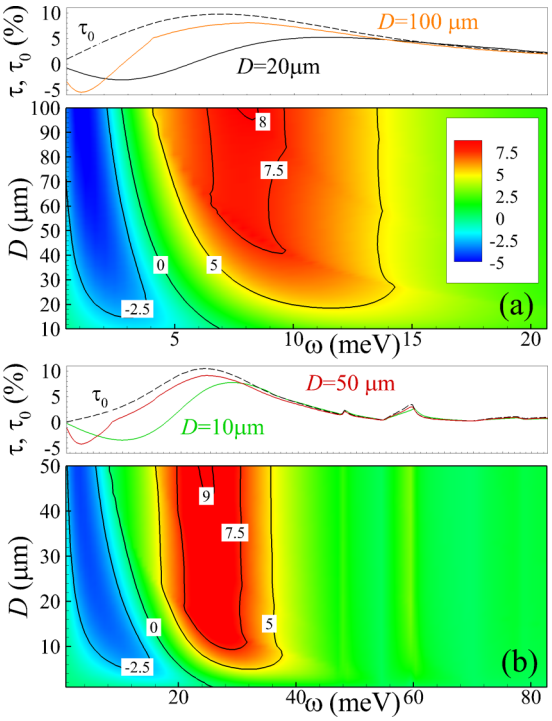

FIG. 9. Coefficient of circular dichroism τ (in percent, depicted by color map) *versus* frequency ω and hole array period D for two values of the magnetic field, $B = 1.5$ T (a) and $B = 7$ T (b). Other parameters of the structure are the same as in Fig. 2. In the upper plots of panels (a) and (b) we trace dependencies $\tau(\omega)$ from the lower plots at fixed values of the hole grating period $D = 20\,\mu$m, $D = 100\,\mu$m [black and orange solid lines in panel (a)], and $D = 10\,\mu$m, $D = 50\,\mu$m [green and red solid lines in panel (b)]. Also in the upper plots of panels (a) and (b) the coefficients of circular dichroism τ_0 of bare graphene are depicted by the dashed black lines.

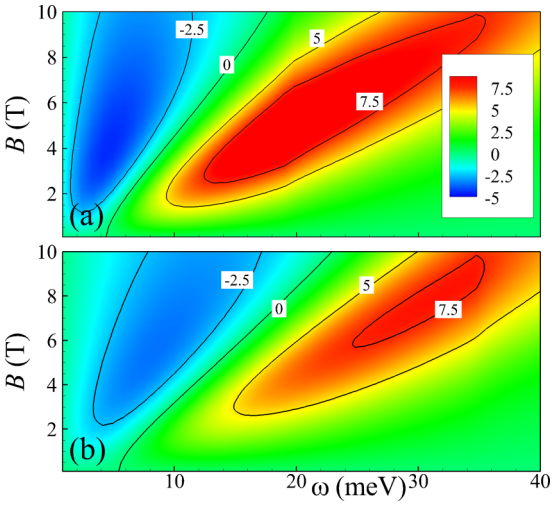

FIG. 10. Coefficient of circular dichroism τ (in percent, depicted by color map) *versus* frequency ω and magnetic field B for two values of the period of the hole array, $D = 20\,\mu$m [panel (a)] and $D = 10\,\mu$m [panel (b)]. Other parameters of the structure are the same as in Fig. 2.

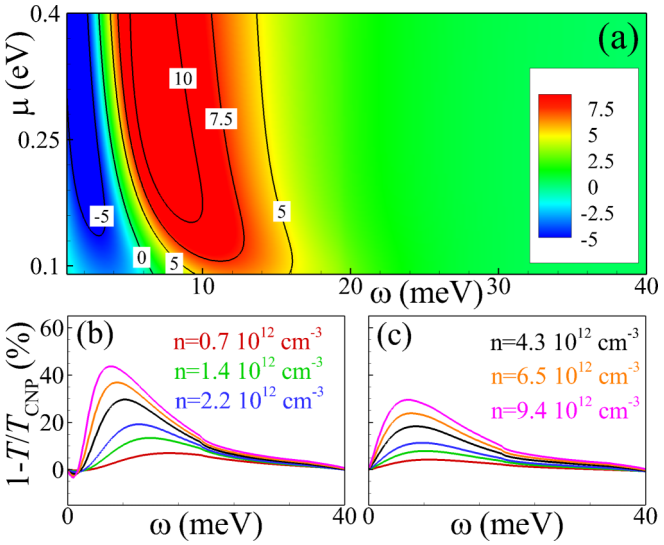

FIG. 11. (a) Coefficient of circular dichroism τ (in percent, depicted by color map) *versus* frequency ω and Fermi energy μ; (b), (c) Frequency dependence of the extinction of the clockwise (b) and counterclockwise (c) circularly polarized electromagnetic wave transmitted through graphene with charge carrier mobility 5000 $\mathrm{cm}^2/\mathrm{Vs}$ and different charge-carrier densities [depicted in panels (b), (c), where color of the text corresponds to the color of the respective line] deposited on a semi-infinite Al_2O_3 substrate. Other parameters of the graphene and perforated metal film are: $B = 1.5$, $D = 20\,\mu$m, $W = 18\,\mu$m, $T = 50$ nm.

(compared to that of clockwise polarized wave) leads to the reduction of the circular dichroism coefficient τ.

Moreover, the presence of the perforated metal film on top of graphene results into the possibility to obtain a negative circular dichroism coefficient (hence, $T_a < T_c$) at the low-frequency region. This situation is in strong contrast with the case of bare graphene without perforated metal film on top of it, where the coefficient of circular dichroism τ_0 is always possitive [$T_a > T_c$, see upper plots in Figs. 9(a) and 9(b)]. It should be stressed that a decrease of the grating period D [as shown in Fig. 9] and an increase of the magnetic field B [see Fig. 10] lead to a broadening of the frequency region with negative τ.

From the other hand, increase of the chemical potential μ results in the narrowing of this region [see Fig. 11(a)]. Also, it leads to a red shift of the region with maximal positive τ. As it can be understood from the comparison of Fig. 11(a) with Figs. 11(b) and 11(c), this red-shift of the maximal τ is accompanied by a red-shift of the maximal extinction for both clockwise and counterclockwise polarization.

[1] M. Faraday, Philos. Trans. Roy. Soc. London **136**, 1 (1846).
[2] G. Gabriel and M. Brodwin, IEEE Trans. Microwave Theory Tech. **13**, 364 (1965).
[3] F. Auracher and H. H. Witte, Opt. Commun. **13**, 435 (1975).
[4] H. Dötsch, N. Bahlmann, O. Zhuromskyy, M. Hammer, L. Wilkens, R. Gerhardt, P. Hertel, and A. F. Popkov, J. Opt. Soc. Am. B **22**, 240 (2005).
[5] L. J. Aplet and J. W. Carson, Appl. Opt. **3**, 544 (1964).
[6] D. Jalas, A. Petrov, M. Eich, W. Freude, S. Fan, Z. Yu, R. Baets, M. Popović, A. Melloni, J. D. Joannopoulos, M. Vanwolleghem, C. R. Doerr, and H. Renner, Nat. Photonics **7**, 579 (2013).
[7] W. B. Ribbens, Appl. Opt. **4**, 1037 (1965).
[8] R. Takei and T. Mizumoto, Jpn. J. Appl. Phys. **49**, 052203 (2010).
[9] P. K. Tien, D. P. Schinke, and S. L. Blank, J. Appl. Phys. **45**, 3059 (1974).
[10] E. Ishida, K. Miura, Y. Shoji, T. Mizumoto, N. Nishiyama, and S. Arai, Jpn. J. Appl. Phys. **55**, 088002 (2016).
[11] Y. Shoji and T. Mizumoto, Sci. Technol. Adv. Mater. **15**, 014602 (2014).
[12] Y. Shoji, K. Miura, and T. Mizumoto, J. Opt. **18**, 013001 (2016).
[13] W. Qiu, Z. Wang, and M. Soljačić, Opt. Express **19**, 22248 (2011).
[14] W. Śmigaj, J. Romero-Vivas, B. Gralak, L. Magdenko, B. Dagens, and M. Vanwolleghem, Opt. Lett. **35**, 568 (2010).
[15] V. Dmitriev and M. N. Kawakatsu, Appl. Opt. **51**, 5917 (2012).
[16] Z. Wang and S. Fan, Opt. Lett. **30**, 1989 (2005).
[17] L. Zhang, D. Yang, K. Chen, T. Li, and S. Xia, Opt. Laser Technol. **50**, 195 (2013).
[18] F. Fan, Z. Guo, J.-J. Bai, X.-H. Wang, and S.-J. Chang, J. Opt. Soc. Am. B **28**, 697 (2011).
[19] Z. Wang, Y. Chong, J. D. Joannopoulos, and M. Soljačić, Nature **461**, 772 (2009).
[20] F. Fan, S.-J. Chang, C. Niu, Y. Hou, and X.-H. Wang, Opt. Commun. **285**, 3763 (2012).
[21] S. Chen, F. Fan, X. Wang, P. Wu, H. Zhang, and S. Chang, Opt. Express **23**, 1015 (2015).
[22] S. Chen, F. Fan, X. He, M. Chen, and S. Chang, Appl. Opt. **54**, 9177 (2015).

[23] E. Ozbay, Science **311**, 189 (2006).
[24] M. I. Stockman, Phys. Today **64**, 39 (2011).
[25] V. V. Temnov, Nat. Photonics **6**, 728 (2012).
[26] G. Armelles, A. Cebollada, A. García-Martín, and M. U. González, Adv. Opt. Mater. **1**, 10 (2013).
[27] I. Maksymov, Nanomaterials **5**, 577 (2015).
[28] K. W. Chiu and J. J. Quinn, Il Nuovo Cimento B **10**, 1 (1972).
[29] V. V. Temnov, G. Armelles, U. Woggon, D. Guzatov, A. Cebollada, A. Garcia-Martin, J.-M. Garcia-Martin, T. Thomay, A. Leitenstorfer, and R. Bratschitsch, Nat. Photonics **4**, 107 (2010).
[30] F. Fan, S. Chen, W. Lin, Y.-P. Miao, S.-J. Chang, B. Liu, X.-H. Wang, and L. Lin, Appl. Phys. Lett. **103**, 161115 (2013).
[31] F. Fan, S.-T. Xu, X.-H. Wang, and S.-J. Chang, Opt. Express **24**, 26431 (2016).
[32] C. J. Firby and A. Y. Elezzabi, Optica **2**, 598 (2015).
[33] A. R. Davoyan and N. Engheta, New J. Phys. **15**, 083054 (2013).
[34] C. J. Firby and A. Y. Elezzabi, Opt. Lett. **41**, 563 (2016).
[35] J. Y. Chin, T. Steinle, T. Wehlus, D. Dregely, T. Weiss, V. I. Belotelov, B. Stritzker, and H. Giessen, Nat. Commun. **4**, 1599 (2013).
[36] B. Caballero, A. García-Martín, and J. C. Cuevas, Opt. Express **23**, 22238 (2015).
[37] V. I. Belotelov, I. A. Akimov, M. Pohl, V. A. Kotov, S. Kasture, A. S. Vengurlekar, A. V. Gopal, D. R. Yakovlev, A. K. Zvezdin, and M. Bayer, Nat. Nanotechnol. **6**, 370 (2011).
[38] L. E. Kreilkamp, V. I. Belotelov, J. Y. Chin, S. Neutzner, D. Dregely, T. Wehlus, I. A. Akimov, M. Bayer, B. Stritzker, and H. Giessen, Phys. Rev. X **3**, 041019 (2013).
[39] S. Xiao, X. Zhu, B.-H. Li, and N. A. Mortensen, Front. Phys. **11**, 117801 (2016).
[40] F. J. García de Abajo, ACS Photon. **1**, 135 (2014).
[41] P.-Y. Chen, C. Argyropoulos, M. Farhat, and J. S. Gomez-Diaz, Nanophotonics **6**, 1239 (2017).
[42] Y. V. Bludov, A. Ferreira, N. M. R. Peres, and M. I. Vasilevskiy, Int. J. Mod. Phys. B **27**, 1341001 (2013).
[43] T. Low and P. Avouris, ACS Nano **8**, 1086 (2014).
[44] F. H. L. Koppens, D. E. Chang, and F. J. García de Abajo, Nano Lett. **11**, 3370 (2011).
[45] A. Y. Nikitin, F. Guinea, F. J. García-Vidal, and L. Martín-Moreno, Phys. Rev. B **84**, 195446 (2011).
[46] K. S. Novoselov, A. K. Geim, S. V. Morozov, D. Jiang, M. I. Katsnelson, I. V. Grigorieva, S. V. Dubonos, and A. A. Firsov, Nature **438**, 197 (2005).
[47] Y. Zhang, Y.-W. Tan, H. L. Stormer, and P. Kim, Nature **438**, 201 (2005).
[48] A. De Martino, L. Dell'Anna, and R. Egger, Phys. Rev. Lett. **98**, 066802 (2007).
[49] M. Tamagnone, A. Fallahi, J. R. Mosig, and J. Perruisseau-Carrier, Nat. Photon. **8**, 556 (2014).
[50] M. Tamagnone, C. Moldovan, J.-M. Poumirol, A. B. Kuzmenko, A. M. Ionescu, J. R. Mosig, and J. Perruisseau-Carrier, Nat. Commun. **7**, 11216 (2016).
[51] R. Shimano, G. Yumoto, J. Y. Yoo, R. Matsunaga, S. Tanabe, H. Hibino, T. Morimoto, and H. Aoki, Nat. Commun. **4**, 1841 (2013).
[52] I. Crassee, J. Levallois, A. L. Walter, M. Ostler, A. Bostwick, E. Rotenberg, T. Seyller, D. van der Marel, and A. B. Kuzmenko, Nat. Phys. **7**, 48 (2010).
[53] D. L. Sounas, H. S. Skulason, H. V. Nguyen, A. Guermoune, M. Siaj, T. Szkopek, and C. Caloz, Appl. Phys. Lett. **102**, 191901 (2013).
[54] O. L. Berman, G. Gumbs, and Y. E. Lozovik, Phys. Rev. B **78**, 085401 (2008).
[55] R. Roldán, J.-N. Fuchs, and M. O. Goerbig, Phys. Rev. B **80**, 085408 (2009).
[56] I. Crassee, M. Orlita, M. Potemski, A. L. Walter, M. Ostler, T. Seyller, I. Gaponenko, J. Chen, and A. B. Kuzmenko, Nano Lett. **12**, 2470 (2012).
[57] H. Yan, Z. Li, X. Li, W. Zhu, P. Avouris, and F. Xia, Nano Lett. **12**, 3766 (2012).
[58] M. Tymchenko, A. Y. Nikitin, and L. Martín-Moreno, ACS Nano **7**, 9780 (2013).
[59] J.-M. Poumirol, P. Q. Liu, T. M. Slipchenko, A. Y. Nikitin, L. Martin-Moreno, J. Faist, and A. B. Kuzmenko, Nat. Commun. **8**, 14626 (2017).
[60] D. A. Kuzmin, I. V. Bychkov, V. G. Shavrov, and V. V. Temnov, Nano Lett. **16**, 4391 (2016).
[61] A. Fallahi and J. Perruisseau-Carrier, Appl. Phys. Lett. **101**, 231605 (2012).
[62] A. Ferreira, J. Viana-Gomes, Y. V. Bludov, V. Pereira, N. M. R. Peres, and A. H. CastroNeto, Phys. Rev. B **84**, 235410 (2011).
[63] The substrate dielectric function includes optical phonon response,

$$\varepsilon_3(\omega) = \varepsilon_\infty + \sum_{n=1}^{4} \frac{f_n \omega_{\mathrm{TO},n}^2}{\omega_{\mathrm{TO},n}^2 - \omega^2 - i\omega\Gamma_{\mathrm{TO},n}}, \qquad \text{(C1)}$$

where $\varepsilon_\infty = 3.2$, $\omega_{\mathrm{TO},1} = 47.7\,\mathrm{meV}$, $\omega_{\mathrm{TO},2} = 54.8\,\mathrm{meV}$, $\omega_{\mathrm{TO},3} = 70.5\,\mathrm{meV}$, $\omega_{\mathrm{TO},4} = 78.7\,\mathrm{meV}$ are phonon frequencies, $\Gamma_{\mathrm{TO},1} = 0.72\,\mathrm{meV}$, $\Gamma_{\mathrm{TO},2} = 0.54\,\mathrm{meV}$, $\Gamma_{\mathrm{TO},3} = 1.41\,\mathrm{meV}$, $\Gamma_{\mathrm{TO},4} = 1.57\,\mathrm{meV}$ are the phonon dampings, and $f_1 = 0.3$, $f_2 = 2.7$, $f_3 = 3.0$, $f_4 = 0.3$ are the weighting coefficients.
[64] The expressions for R_0 and T_0 as well as the details of derivation can be found in Appendix B 2.
[65] M. Born and E. Wolf, *Principles of Optics*, 7th ed. (Cambridge University Press, Cambridge, 1999).
[66] Excepting narrow frequency windows at $55\,\mathrm{meV} \lesssim \omega \lesssim 60\,\mathrm{meV}$, and $72\,\mathrm{meV} \lesssim \omega \lesssim 75\,\mathrm{meV}$, where, nevertheless, an increase of the Faraday rotation angle is negligibly small.
[67] P. K. Basu, *Theory of Optical Processes in Semiconductors* (Clarendon Press, Oxford, 1997).
[68] Alternatively, it can be quantified in terms of the coefficient of circular dichroism introduced in Appendix C.
[69] E. J. C. Dias and N. M. R. Peres, ACS Photon. **4**, 3071 (2017).
[70] T. W. Ebbesen, H. J. Lezec, H. F. Ghaemi, T. Thio, and P. A. Wolff, Nature **391**, 667 (1998).